Monthly Notices of the ROYAL ASTRONOMICAL SOCIETY

MNRAS **527,** 1612–1632 (2024) https://doi.org/10.1093/mnras/stad3223
Advance Access publication 2023 October 21

Feedback-driven anisotropy in the circumgalactic medium for quenching galaxies in the SIMBA simulations

Tianyi Yang [1]★ Romeel Davé [1,2]★ Weiguang Cui [1,3]★ Yan-Chuan Cai,[1] John A. Peacock [1] and Daniele Sorini [1,4,5]

[1]*Institute for Astronomy, University of Edinburgh, Royal Observatory, Blackford Hill, Edinburgh EH9 3HJ, UK*
[2]*Department of Physics and Astronomy, University of the Western Cape, Bellville, Cape Town 7535, South Africa*
[3]*Departamento de Física Teórica and CIAFF, Modulo 8 Universidad Autónoma de Madrid, E-28049 Madrid, Spain*
[4]*Institute for Computational Cosmology, Durham University, South Park Road, Durham DH1 3LE, UK*
[5]*Département de Physique Théorique, Université de Genève, 24 quai Ernest Ansermet, CH-1211 Genève 4, Switzerland*

Accepted 2023 October 17. Received 2023 October 2; in original form 2023 May 1

ABSTRACT

We use the SIMBA galaxy formation simulation suite to explore anisotropies in the properties of circumgalactic gas that result from accretion and feedback processes. We particularly focus on the impact of bipolar active galactic nuclei (AGNs) jet feedback as implemented in SIMBA , which quenches galaxies and has a dramatic effect on large-scale gas properties. We show that jet feedback at low redshifts is most common in the stellar mass range (1–5) $\times$ 10^{10} $M_\odot$, so we focus on galaxies with active jets in this mass range. In comparison to runs without jet feedback, jets cause lower densities and higher temperatures along the galaxy minor axis (SIMBA jet direction) at radii $\gtrsim 0.5r_{200c} - 4r_{200c}$ and beyond. This effect is less apparent at higher or lower stellar masses, and is strongest within green valley galaxies. The metallicity also shows strong anisotropy out to large scales, driven by star formation feedback. We find substantially stronger anisotropy at $\lesssim 0.5r_{200c}$, but this also exists in runs with no explicit feedback, suggesting that it is due to anisotropic accretion. Finally, we explore anisotropy in the bulk radial motion of the gas, finding that both star formation and AGN wind feedback contribute to pushing the gas outwards along the minor axis at $\lesssim 1$ Mpc, but AGN jet feedback further causes bulk outflow along the minor axis out to several Mpc, which drives quenching via gas starvation. These results provide observational signatures for the operation of AGN feedback in galaxy quenching.

Key words: methods: numerical – galaxies: evolution – galaxies: formation – galaxies: general – galaxies: jets.

1 INTRODUCTION

The circumgalactic medium (CGM) is the gaseous environment surrounding a galaxy, which can extend up to hundreds of kpc from the galactic centre. The CGM is closely related to the process of galaxy evolution because it is the site where galactic inflows and outflows interplay (see e.g. Tumlinson, Peeples & Werk 2017, and references therein). Cold gas in the CGM accretes on to the central galaxy, fuelling future star-forming activity. Meanwhile, gas can be carried out into the CGM by galactic-scale outflows, which causes gas depletion in the central regions and results in suppression of star formation there. These outflows can be driven by stellar feedback in low-mass galaxies, feedback from active galactic nuclei (AGNs) in high-mass galaxies, or even a combination of the two mechanisms (see e.g. Somerville & Davé 2015, and references therein).

AGN feedback effects, which are sourced by gas accretion on to supermassive black holes (SMBH), are known to be a major source of energy input to the CGM. AGN feedback is thought to be an important ingredient in regulating the growth of central black holes and suppressing the star-forming activity in galaxies (e.g. Guillard et al. 2015; Harrison 2017; Morganti 2017). According to observations, SMBH exist at the centres of most massive galaxies (see e.g. Kormendy & Ho 2013, and references therein), and the AGN feedback mechanisms appear in two modes: 'quasar' and 'radio' mode (see e.g. Ho 2008; Fabian 2012; Heckman & Best 2014). The 'quasar' mode is found in luminous AGN with high accretion rates. In this case, the feedback energy is released into the surroundings in the form of radiation from the central accretion disc, which can drive powerful winds. The 'radio' mode is usually found in galaxies hosting AGNs with low accretion rates. These are radiatively inefficient but are capable of releasing large amounts of feedback energy into the CGM by means of bubbles or radio jets. Relatively clear observational evidence exists for AGN feedback in action (e.g. Maiolino et al. 2012), and results from SIMBA simulations have suggested that this mechanism is key to the quenching of galaxies (Cui et al. 2021). Nevertheless, much remains to be understood about the detailed operation of these processes, and in particular how they interact with the CGM.

Hydrodynamical simulations provide opportunities for studying how AGN feedback reshapes the properties and evolution of the CGM. To reproduce various observed galaxy properties, it is necessary to include the modelling of AGN feedback in simulations:

★ E-mail: s2109053@ed.ac.uk (TY); romeel.dave@ed.ac.uk (RD); cuiweiguang@gmail.com (WC)

this enables suppression of star formation in massive galaxies and prevents them undergoing excessive growth (Le Brun et al. 2014; Schaye et al. 2015; Sijacki et al. 2015; McCarthy et al. 2017; Cui et al. 2018; Weinberger et al. 2018; Davé et al. 2019). AGN feedback is also important in allowing simulations to reproduce other observed thermodynamic and chemical properties of the gas, such as the hot gas fraction in groups and CGM metal absorption line properties (McCarthy et al. 2010; Davé et al. 2019; Oppenheimer et al. 2021; Cui et al. 2022).

Although simulations have successfully reproduced a wide range of observed galaxy properties, the implementations of SMBH feedback in different codes are distinct in a number of ways. Regarding the form of feedback energy, there are two major ways of implementing this: either by heating up the surrounding gas isotropically with the expected amount of energy from the AGNs (e.g. in cosmo-OWLS and EAGLE simulations: Le Brun et al. 2014; Schaye et al. 2015), or by ejecting gas particles with kinetic kicks along a random or bipolar direction (e.g. in IllustrisTNG and SIMBA simulations: Weinberger et al. 2018; Davé et al. 2019). Both mechanisms succeed in matching galaxy observations, but the way in which the released energy propagates into the CGM must be different. This may have a strong impact on the properties of the CGM and thus produce distinctive observable features in the resulting CGM gas distribution.

The interplay between galactic feedback outflows and the CGM has been widely studied in both observations and simulations, over a large range of redshifts and stellar masses. This includes, for example: the distribution of highly ionized gas such as oxygen (e.g. Nelson et al. 2018; Kakkad et al. 2020); the abundance of Mg II-traced cold gas (e.g. Bordoloi et al. 2011; Bouché et al. 2012; Kacprzak, Churchill & Nielsen 2012; Nielsen et al. 2015; Nelson et al. 2021); emission lines such as 21 cm and Hα (e.g. Putman, Peek & Joung 2012; Kakkad et al. 2023); the warm diffuse gas via the thermal Sunyaev–Zeldovich (tSZ) effect (e.g. Lokken et al. 2022; Orlowski-Scherer et al. 2022; Yang et al. 2022); Ly α and metal absorption lines (e.g. Meiksin, Bolton & Tittley 2014; Turner et al. 2014; Meiksin, Bolton & Tittley 2015; Meiksin, Bolton & Puchwein 2017; Turner et al. 2017; Sorini et al. 2018; Sorini, Davé & Anglés-Alcázar 2020; Appleby et al. 2021, 2023); and the hot dense atmosphere probed by X-rays (e.g. Truong et al. 2020; Truong, Pillepich & Werner 2021a; Truong et al. 2021b). In particular, some observations have shown that, for disc-dominated galaxies, galactic outflows emerging from the disc are preferentially ejected biconically into the CGM, where the strongest outflow features are captured along the minor axis of the disc (e.g. in Bordoloi et al. 2011; Bouché et al. 2012). Infalling gas is preferentially accreted in the galaxy plane (e.g. in Bouché et al. 2013; Nielsen et al. 2015). For red passive galaxies, however, their CGM distribution tends to be more isotropic (e.g. in Kacprzak, Churchill & Nielsen 2012; Nielsen et al. 2015). In simulations, although different feedback models are implemented, this type of angular dependence is also widely found (e.g. Mitchell et al. 2020; Péroux et al. 2020; Pillepich et al. 2021). These studies suggest that the CGM properties connect closely to the feedback activity inside galaxies. Specifically, outflow features in the CGM are generally more prominent along the minor axis of the disc (edge-on projection), and accretion is more easily observed along the galaxy disc (face-on projection).

However, the detailed outflow features and their angular dependence are quite sensitive to the adopted AGN feedback model, which in turn affects the predicted CGM distribution and the galaxy evolution processes. In particular, the outflow angular dependence and the predicted CGM properties can differ significantly in the EAGLE and TNG simulations (Nelson et al. 2019; Davies et al. 2020; Mitchell et al. 2020). Under the TNG framework, Pillepich et al. (2018) and Terrazas et al. (2020) found that the resulting $M_{\rm BH}$–M_*–sSFR relation of galaxies depends strongly on the chosen parameters of the AGN feedback model in TNG. They further confirmed that kinetic wind feedback is required in order to reproduce a quiescent galaxy population that is consistent with observations. Furthermore, the CGM anisotropic features can be altered by the form of released energy, depending on whether the kinetic or the thermal feedback mode dominates around galaxies (Zinger et al. 2020; Ramesh, Nelson & Pillepich 2023). The sensitivity of CGM anisotropy to AGN models has been further discussed by comparing results predicted from simulations to observations, such as the X-ray hardness (Truong et al. 2021b) and the satellite distribution around their centrals (Martín-Navarro et al. 2021). Therefore, by studying the feedback-driven anisotropy in the CGM, we aim to identify and predict the observational consequences owing to feedback. This provides possible ways to constrain AGN models with further observations, which is a crucial step towards understand how galaxies evolve and undergo quenching.

In this paper, we focus on the anisotropic behaviour of the CGM and its relation to jet activity using SIMBA simulations, including in particular different runs with various feedback models turned on/off. We study the spatial CGM distribution around central galaxies by stacking a large sample of simulated galaxies. The CGM anisotropy is quantified by the quadrupole moments of various physical quantities, and we further examine the dependence of these signals on the implemented AGN models, central galaxy mass and star formation status. Finally, we explore the anisotropy in gas radial motion and the redshift evolution of the feedback-driven anisotropic features. These provide us insight into how different feedback mechanisms regulate galactic outflow and eventually drive galaxy quenching under the SIMBA framework.

The paper is organized as follows. We first introduce a brief summary of the SIMBA simulation suits, especially the implemented feedback models, as well as our methodology in Section 2. Then in Section 3, we present our main anisotropic results regarding the CGM properties considered in this work: mass, density, metallicity, and thermal pressure. Around SIMBA -100 central galaxies, we study how the angular dependence of CGM distribution varies with their host properties, such as star formation status (Section 3.1) and mass (Section 3.2). Then in Section 3.3, we present the effect of feedback models on the resulting CGM properties, using SIMBA -50 model variants. In Section 4, by exploring the bulk radial gas motion around SIMBA -50 galaxies (Section 4.1) and by tracing progenitors of $z = 0.0$ quenched samples (Section 4.2), we discuss the connection of AGN feedback models in SIMBA -50 variants and further see what drives galaxy quenching in SIMBA model. We discuss and summarize our main findings in Sections 5–7.

2 METHODOLOGY

We begin with an overview of the SIMBA simulations in Section 2.1. Owing to its importance for this work, we summarize the modelling of black hole feedback adopted in SIMBA models in Section 2.2. We move on to the selection of galaxies in Section 2.3, and finally introduce our methodology used to characterize the anisotropy of CGM properties in Sections 2.4 and 2.5.

2.1 The SIMBA simulations

SIMBA (Davé et al. 2019) is a suite of hydrodynamic simulation using the GIZMO code (Hopkins 2015). Dark matter and gas particles are evolved within a periodic cubical volume with

a cosmology broadly concordant with *Planck* 2015 (Planck Collaboration XIII 2016): $\Omega_{m,0} = 0.3$, $\Omega_{\Lambda,0} = 0.7$, $\Omega_{b,0} = 0.048$, $H_0 = 68\,\mathrm{km\,s^{-1}\,Mpc^{-1}}$, $\sigma_8 = 0.82$, and $n_s = 0.97$. The fiducial run (denoted SIMBA-100) has a box length of 100 comoving h^{-1} Mpc (hereafter h^{-1} cMpc), evolving from $z = 249$ to $z = 0$ with 1024^3 dark matter particles and 1024^3 gas elements. To explore the variation of anisotropic features with input feedback models, there are several $50\,h^{-1}$ cMpc boxes (denoted SIMBA-50) using 512^3 dark matter particles and 512^3 gas elements. The mass resolution for both cases is $1.82 \times 10^7\,\mathrm{M_\odot}$ for gas cells and $9.58 \times 10^7\,\mathrm{M_\odot}$ for dark matter particles. The initial conditions for all SIMBA runs are identical for a given box size.

In SIMBA, star formation is modelled using an H_2−based star formation rate. This is given by the H_2 density divided by the dynamical time with $\mathrm{SFR} = \epsilon_* \rho_{H_2}/t_{\rm dyn}$, where $\epsilon_* = 0.02$ (Kennicutt 1998). The H_2 fraction is calculated using the subgrid model of Krumholz & Gnedin (2011) based on the metallicity and local column density, with some minor modifications to account for the variations in numerical resolution (Davé, Thompson & Hopkins 2016). The chemical enrichment model tracks eleven elements in total (H, He, C, N, O, Ne, Mg, Si, S, Ca, Fe) from Type II supernovae (SNe), Type Ia SNe, and asymptotic giant branch (AGB) stars. The star formation-driven galactic winds are modelled as decoupled two-phase metal-loaded winds, with 30 per cent of ejected wind particles being hot and with a redshift-independent mass loading factor that scales with stellar mass (Anglés-Alcázar et al. 2017b). The SF wind velocity, modified from the scaling in Muratov et al. (2015), is computed via the following equation:

$$v_w = 1.6 \left(\frac{v_c}{200\,\mathrm{km\,s^{-1}}}\right)^{0.12} v_c + \Delta v(0.25 R_{\rm vir}), \quad (1)$$

where v_c is the galaxy's circular velocity at $0.25R_{\rm vir}$, and $\Delta v(0.25R_{\rm vir})$ is an extra velocity kick corresponding to the gravitational potential difference between the wind launch radius and $0.25R_{\rm vir}$ (Łokas & Mamon 2001).

Black holes are seeded and grown during the simulation, and the accretion energy drives feedback that causes star formation to become quenched. Black hole growth in SIMBA is modelled with a two-mode accretion model. For cold gas with $T < 10^5$K, the gas inflow is implemented using the torque-limited accretion model (Anglés-Alcázar et al. 2017a). While hot gas ($T > 10^5$K) is accreted on to black holes via Bondi accretion (Bondi 1952). The major improvement of the black hole growth model adopted by SIMBA is the torque-limited accretion for the cold gas, which does not require the black hole to self-regulate its own growth (Anglés-Alcázar et al. 2015). This allows for the implementation of a more physical AGN feedback model, which will be discussed in Section 2.2. Other input physical mechanisms such as radiative cooling and heating, the formation and evolution of dust are also included in SIMBA runs. Specifics of these models are available in Davé et al. (2019).

2.2 Black hole feedback models in SIMBA

AGN feedback is responsible for quenching galaxies in SIMBA. It is implemented by a two-mode model, which is motivated by the observed dichotomy in black hole growth (e.g. in Heckman & Best 2014). A 'radiative mode' is applied when a black hole is accreting at high Eddington ratios ($f_{\rm Edd} = \dot{M}_{\rm BH}/\dot{M}_{\rm Edd}$), which mimics the molecular and warm ionized gas outflow (Perna et al. 2017a). AGN wind particles are ejected without modifications of the gas temperature, with a typical electron temperature of $\sim 10^4$ K and with a velocity of $\sim$ 1000 km s^{-1} (Perna et al. 2017b). In this case, the outflow velocity is related to the black hole mass via:

$$v_{w,\rm EL} = 500 + 500(\log_{10} M_{\rm BH} - 6)/3\,\mathrm{km\,s^{-1}}. \quad (2)$$

While at low Eddington ratios, a 'jet mode' is applied to drive high-velocity hot gas outflows (Fabian 2012). The jet direction is set parallel/antiparallel to the inner gas disc of the host galaxy. Its angular momentum vector is computed using the 256 closest gas particles around the central black hole (typically $\sim$1 kpc), with an upper limit of $R_{\rm inner\ disk} \leq 2\,h^{-1}$ ckpc. Gas particles are heated to the virial temperature of the halo before ejection and the velocity becomes stronger as $f_{\rm Edd}$ drops:

$$v_{w,\rm jet} = v_{w,\rm EL} + 7000 \log_{10}(0.2/f_{\rm Edd})\ \mathrm{km\,s^{-1}}. \quad (3)$$

The transition between radiative and jet mode happens when black holes have $f_{\rm Edd} < 0.2$ and $M_{\rm lim,BH} \geq 10^{7.5}\,\mathrm{M_\odot}$. The velocity increase is capped at 7000 km s^{-1} above $v_{w,\rm El}$ when $f_{\rm Edd} \leq 0.02$.

Finally, X-ray heating by the accretion disc is also included by SIMBA when its jet model is turned on and gas fractions within the black hole kernel are below 0.2, as motivated by Choi et al. (2012). This mimics the deposition of high-energy photons into the surrounding gas and is implemented in two modes: for non-ISM gas (with hydrogen number density of $n_{\rm H} < 0.13\,\mathrm{cm^{-3}}$), gas temperature values are directly increased based on the local radiation flux. For ISM gas, half of the radiation energy is applied as a radial kick outwards to gas particles, while the remainder is added as heat. X-ray feedback causes only modest changes to the galaxy stellar mass function, but it is crucial in order to achieve full quenching of the star formation in massive galaxies (see section 4 in Davé et al. 2019).

There are several model variants implemented in the SIMBA-50 run: 'allphys', which includes all the aforementioned physics identical to the SIMBA-100 fiducial run; 'nojet', which turns off the bipolar jet and X-ray feedback; 'noagn', which only includes stellar feedback but with all AGN feedback turned off; 'nox', which only turns off the X-ray feedback; and 'nofb', where all explicit feedback is turned off. A brief description and summary of these models is given in Table 1. In Section 3.3, we show a comparison of our results for various different SIMBA-50 runs when discussing the sensitivity of CGM properties to the physics models. After convergence tests between SIMBA-50-'allphys' and the SIMBA-100 run (Appendix A), we thereafter include results from SIMBA-100 only, where more samples are available for further analysis.

Table 1. Feedback descriptions for different SIMBA-50 runs. Note that the SIMBA-100 fiducial run employs the same 'allphs' model as the SIMBA-50 run.

Model	Stellar feedback	AGN radiative mode	AGN jet mode[a]	X-ray heating
'allphys'	✓	✓	✓, with $f_{\rm Edd}^{b}$ and $M_{\rm BH,\,lim}$ cut[c]	✓, coupled with jet
'nox'	✓	✓	✓	x
'nojet'	✓	✓	x	x
'noagn'	✓	x	x	x
'nofb'	x	x	x	x

[a]The criteria for the jet AGN feedback to be turned on are $f_{\rm Edd}$ [b] and $M_{\rm BH}$ [c]. Full jet speed is achieved when $f_{\rm Edd} < 0.02$, see equation (3).
[b] $f_{\rm Edd} < 0.2$.
[c] $M_{\rm BH} \geq M_{\rm BH,lim} = 10^{7.5}\,\mathrm{M_\odot}$.

2.3 Galaxy selection

The main sample considered in this study consists of the galaxies at $z = 0$ that are central, have black hole accretion rate >0 and stellar mass $>10^{10}$ M$_\odot$. In this work, stellar mass (denoted by M_*) is defined as the total mass of stellar particles within 30 ckpc spherical apertures. The choice of this stellar mass cut is adopted owing to the AGN fraction$-M_*$ plot from the simulations (Fig. 1, which is discussed later) as well as from observations (e.g. Kauffmann et al. 2003), which suggest that the strong AGN fraction declines significantly below $M_* = 10^{10}$ M$_\odot$. We also divide our main sample into the following sub-catalogues when necessary:

(i) *'Jet-active' galaxies*. For a better visualization of the anisotropic features, we also analyse galaxies with low Eddington accretion ratio and high central black hole mass ($0 < f_{\rm edd} < 0.02$, $M_{\rm BH} \geq 10^{7.5}$ M$_\odot$). As discussed in Section 2.2, these are the criteria adopted in the 'allphys' model when full jet speeds are achieved. Note that we will use the term 'jet-active galaxies' to refer exclusively to galaxies that have jets with the full jet speeds. This is only meaningful in the 'allphys' or 'nox' models when a jet is implemented. For other models that have no jets, but comparing with simulations run with the same initial conditions as in the 'allphys' model, we can identify galaxies that are the counterparts of those in the 'allphys' simulations. We will refer to these galaxies as 'jet-active counterparts'.

(ii) *Galaxy type*. Galaxies are categorized into star-forming (SF), green valley (GV) and quenched (Q) galaxies based on the observed star-forming main sequence (SFMS) in Belfiore et al. (2018). Their best-fitting line is given by

$$\log({\rm SFR}/{\rm M}_\odot{\rm yr}^{-1}) = 0.73\,\log(M_*/{\rm M}_\odot) - 7.33, \quad (4)$$

with a scatter of 0.39 dex. According to this line, the lower boundary of SF galaxies is the upper dashed white line shown in Fig. 1, which is 1σ below the best-fitting SFMS line. GV galaxies are defined as having SFR values down to 1 dex below this line. Quenched galaxies are therefore all samples below the GV region. To account for the redshift evolution of the main sequence, we empirically boost their normalization by a factor of $(1 + z)^2$ when considering $z > 0$.

Fig. 1 shows the SFR$-M_*$ plots for all central galaxies in SIMBA-100 at three different redshifts ($z = 1.0, 0.5$, and 0.0), overplotted with the jet-active ratio and number contours of main sample galaxies. Jet-active ratio is defined as the ratio between the numbers of galaxies in the 'jet-active' sample and in the main sample, per SFR$-M_*$ bin. Galaxies are demarcated as SF, GV, and Q based on the boundary lines discussed above. Vertical dashed lines group the galaxies into three stellar mass bins that will be considered in this study. We will show in this study that AGN jet feedback causes more galaxies to enter into the GV region as time evolves, and these eventually become quenched. Furthermore, at all redshifts the majority of 'jet-active' galaxies reside in the GV region with 10^{10} M$_\odot$ $< M_* <$ 5×10^{10} M$_\odot$, suggesting that the efficiency of jet production peaks for these galaxies. This is also broadly consistent with observations (e.g. in Nandra et al. 2007; Schawinski et al. 2007; Pović et al. 2012).

Additionally, we further include an analysis regarding how the anisotropic features evolved with redshift. We will discuss the sample selection of this analysis below.

2.4 Gas properties around galaxies via stacking

Since the results obtained from individual galaxies can be noisy, maps of gas properties are combined together via stacking. Mean galaxy properties are evaluated in either edge-on or face-on projections. These are then rotated with respect to the minor axes of their inner gas discs – which is the assumed jet direction (see the definition in Section 2.2), as well as using all gas particles within a cube of size $4 \times r_{200c}$. Here, r_{200c} is our adopted definition of the virial radius: the radius within which the mean density is 200 times the critical density. Therefore, edge-on projection is when the vertical direction is aligned along the minor axes of the galaxies, while the face-on projection is when viewing the galaxies along the plane of their 'inner discs'. We deliberately chose to stack galaxies along this direction because this is the bipolar feedback direction as defined in the SIMBA-'allphys' model, where one should in principle 'observe' the most anisotropic features in the stacked map if there are any. For comparison, we also repeat the same analysis by stacking galaxies along their stellar angular momentum directions, as discussed in Appendix B. This does not affect the anisotropic features of the CGM properties.

For the projection, particle column densities are derived by summing along the line of sight, while averaged quantities such as gas temperature and metallicity are computed in a mass-weighted manner along the line of sight. Gas metallicity is converted into solar units by dividing by the solar metal mass fraction, for which we use 0.0127. Only non star-forming gas cells are selected while analysing CGM gas properties. To highlight the spatial anisotropy of the CGM properties, we further normalize the stacked map with respect to the azimuthal average. All maps have a resolution of 500×500 pixels. The coordinates are standardized such that all galaxies have the same size in units of the virial radius while stacking. The resolution in physical units corresponds to ~ 3.2 ckpc at the lowest stellar mass bin (with $M_* = 1 \times 10^{10}$–5×10^{10}M$_\odot$) and ~ 6.5 ckpc at the highest mass bin (with $M_* > 1 \times 10^{11}$ M$_\odot$).

Fig. 2 shows the edge-on maps of CGM properties around central 'jet-active' galaxies selected from SIMBA-50-'allphys' at $z = 0$, for the lowest stellar mass bin. We present the gas temperature $T_{\rm mw}$, gas column density $\Sigma_{\rm gas}$, expected SZ$-y$ signal and dark matter column density $\Sigma_{\rm DM}$ on the map. From these maps, it is obvious that the CGM distribution is bipolar, with the direction of the pole being aligned with the direction of the jet.

2.5 Characterizing the anisotropy

In our study, the angular location of the CGM is defined with respect to the minor axis of inner gas disc (Section 2.4). Therefore, an azimuthal angle of 0° denotes alignment with the minor axis, where for models with AGN feedback turned on this is identical to the outflow direction. We first average the four quadrants of the stacked maps (e.g. Fig. 2), assuming that no distinctive features are present in any particular quadrant. Then, to characterize the angular dependence of the CGM properties, we compute the quadrupole moment of CGM properties in the stacked map as follows:

$$\xi^r_\ell(r) = \int_0^1 \xi(r,\mu)(1+2\ell)P_\ell(\mu)\,d\mu, \quad (5)$$

where $\xi(r, \mu)$ is some property of the CGM; $\ell = 2$; $\mu = \cos\theta = y_{\rm corr}/r$; $\mu = 1$ corresponds to angular alignment with the minor axis; r is the 2D projected distance from the galactocentric centre; and $P_\ell(\mu)$ are the Legendre polynomials with $P_2(\mu) = \frac{1}{2}(3\mu^2 - 1)$. If the CGM distribution $\xi(r, \mu)$ is purely isotropic around galaxies, the above integration yields zero. Otherwise, it yields a positive value if the CGM tends to be distributed closer to the minor axis, or a negative value if the distribution is along the galaxy plane (a disc-like feature). We will denote these measured quadrupole moments with a subscript according to the quantity of interest: ξ_T for the projected CGM temperature etc.

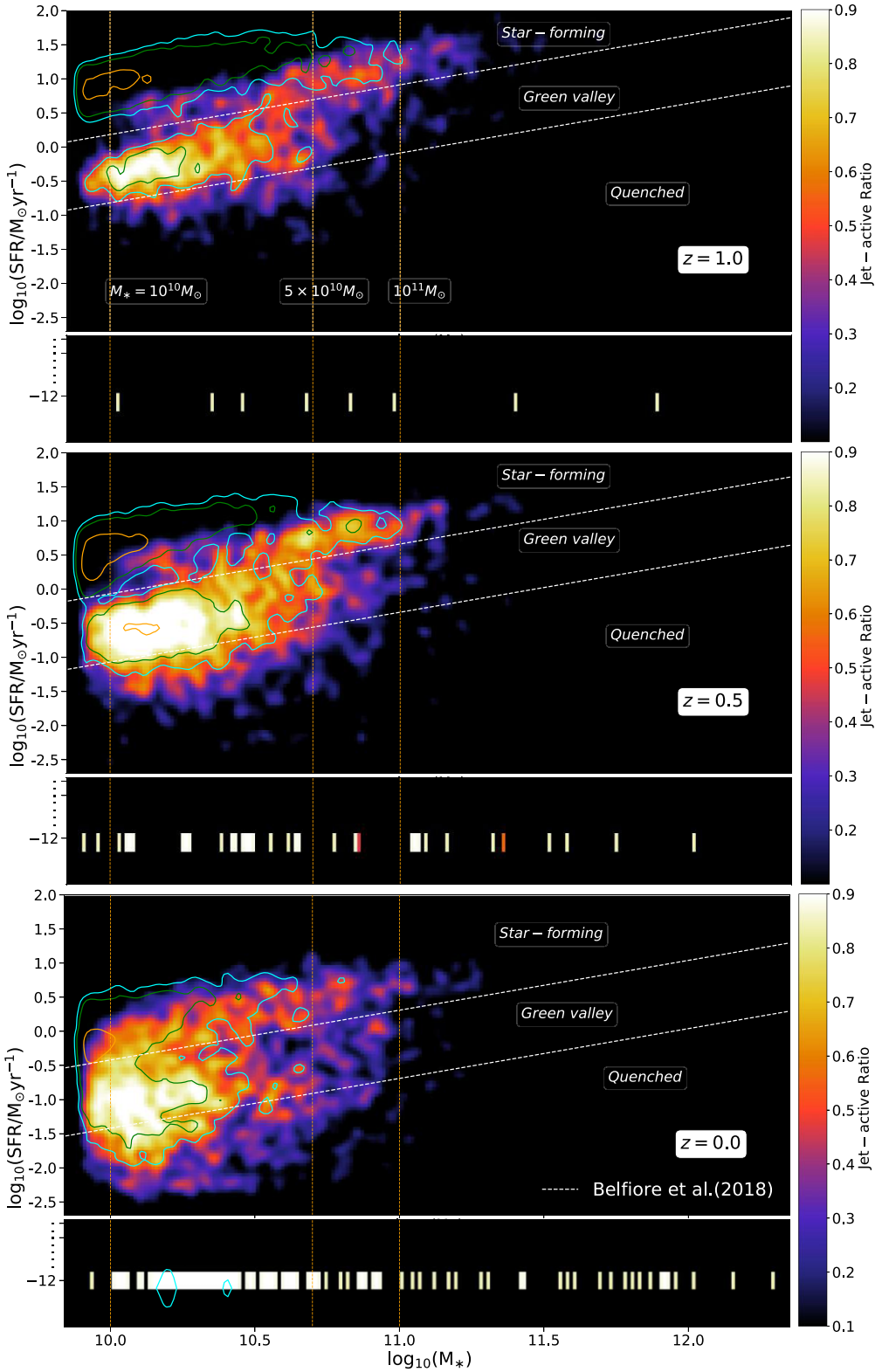

Figure 1. Star formation rate versus stellar mass relation for all central galaxies (the main sample) in the SIMBA-100 run at $z = 1.0$ (*top*), 0.5 (*middle*), and 0.0 (*bottom*). The colourbar shows the jet-active ratio at different redshifts (as defined in Section 2.3). Contours present the number distribution of main sample galaxies with $M_* \geq 10^{9.9}$. This lower M_* cut is empirically chosen so that the contours overlap with the colourmap. Regions of SF, GV, and Q galaxies are demarcated by the white dashed lines, which are the selection criteria adopted by Belfiore et al. (2018) (see text for details). Vertical dashed lines divide the galaxies into three stellar mass bins that will be considered in further analysis below. It is noticeable that at all redshifts, 'jet-active' galaxies are the most populous within the GV region between $M_* = 10^{10}$ $\mathrm{M}_\odot$ and 5×10^{10} $\mathrm{M}_\odot$.

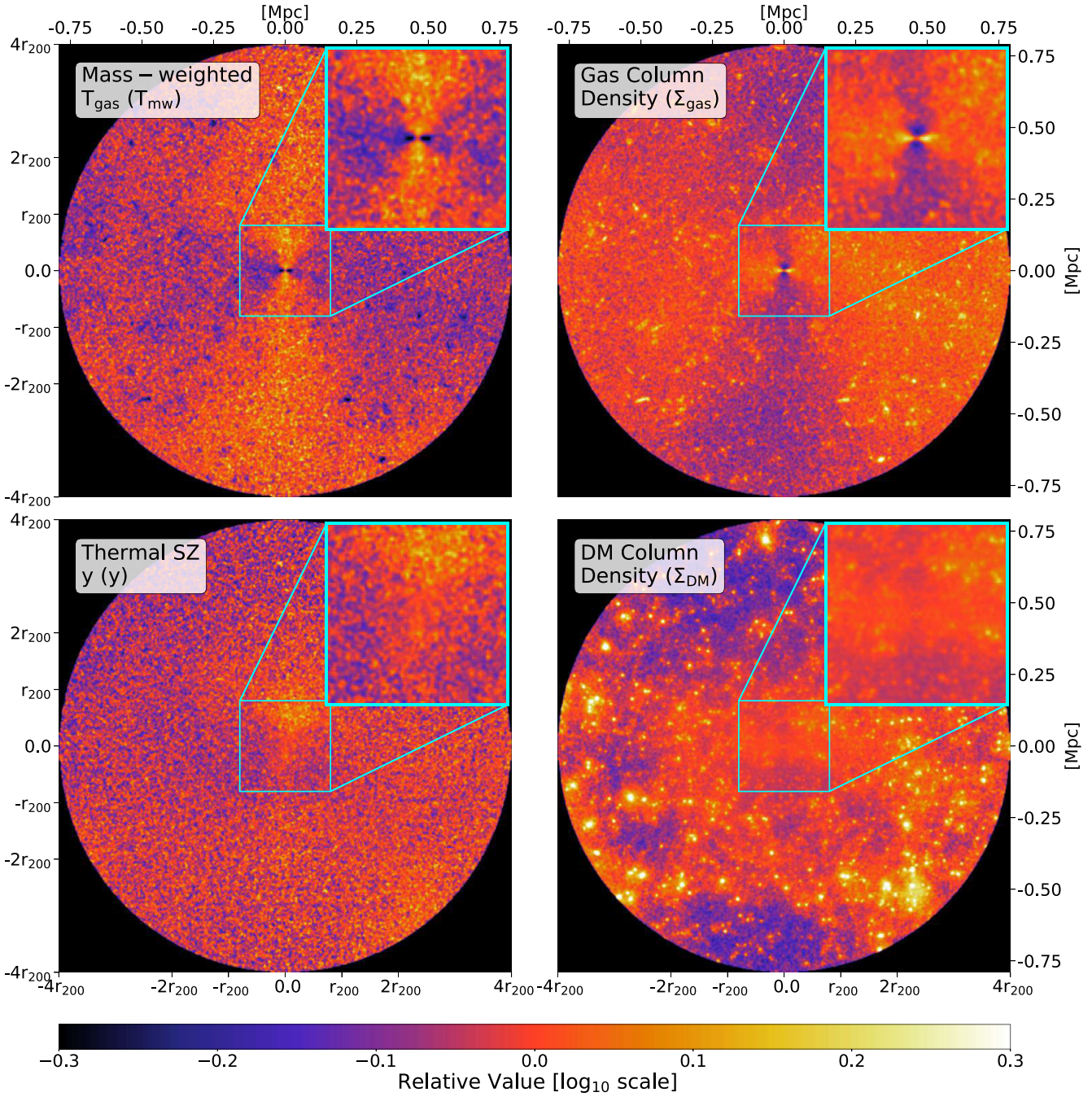

Figure 2. Anisotropy of the CGM properties for 'jet-active' central galaxies at $z = 0.0$ (edge-on view). Galaxies are selected from the SIMBA −50-'allphys' model with stellar mass between 1×10^{10} and 5×10^{10} $M_\odot$. There are 377 galaxies in total and the averaged host halo mass is $\langle \log_{10}(M_{200c}) \rangle = 12.04$. *Top row*: mass-weighted temperature map (T_{mw}, *left*) and gas column density map (Σ_{gas}, *right*). *Bottom row*: thermal SZ y map (SZ−y, *left*) and dark matter column density map (Σ_{dm}, *right*). Maps are normalized with respect to the azimuthal average. Minor axes of galaxies are aligned along the inner disc momentum directions (jet directions in this case), as well as all particles within a cubic region of $\pm 4r_{200c}$. Note that the topmost and leftmost coordinates are in units of cMpc for comparison. On each panel, the small window in the upper right corner zooms into the central square region with size r_{200c}.

3 ANISOTROPIC DISTRIBUTION OF CGM IN SIMULATIONS

We expect the CGM properties to be regulated by AGN feedback processes, which is also connected to the host galaxies of the AGN, and possibly also their host dark matter haloes. In this section, we investigate how the CGM anisotropy is connected to the host galaxy properties, i.e. star formation status (Section 3.1) and host halo mass (Section 3.2). In Section 3.3, we investigate how the distribution of CGM properties varies with the implemented SIMBA -50 feedback models. Note that our definition of CGM is broad – not restricted to the gas within the virial radius, but including all gas outside the virial radius that is connected to the physical activity in the central galaxies.

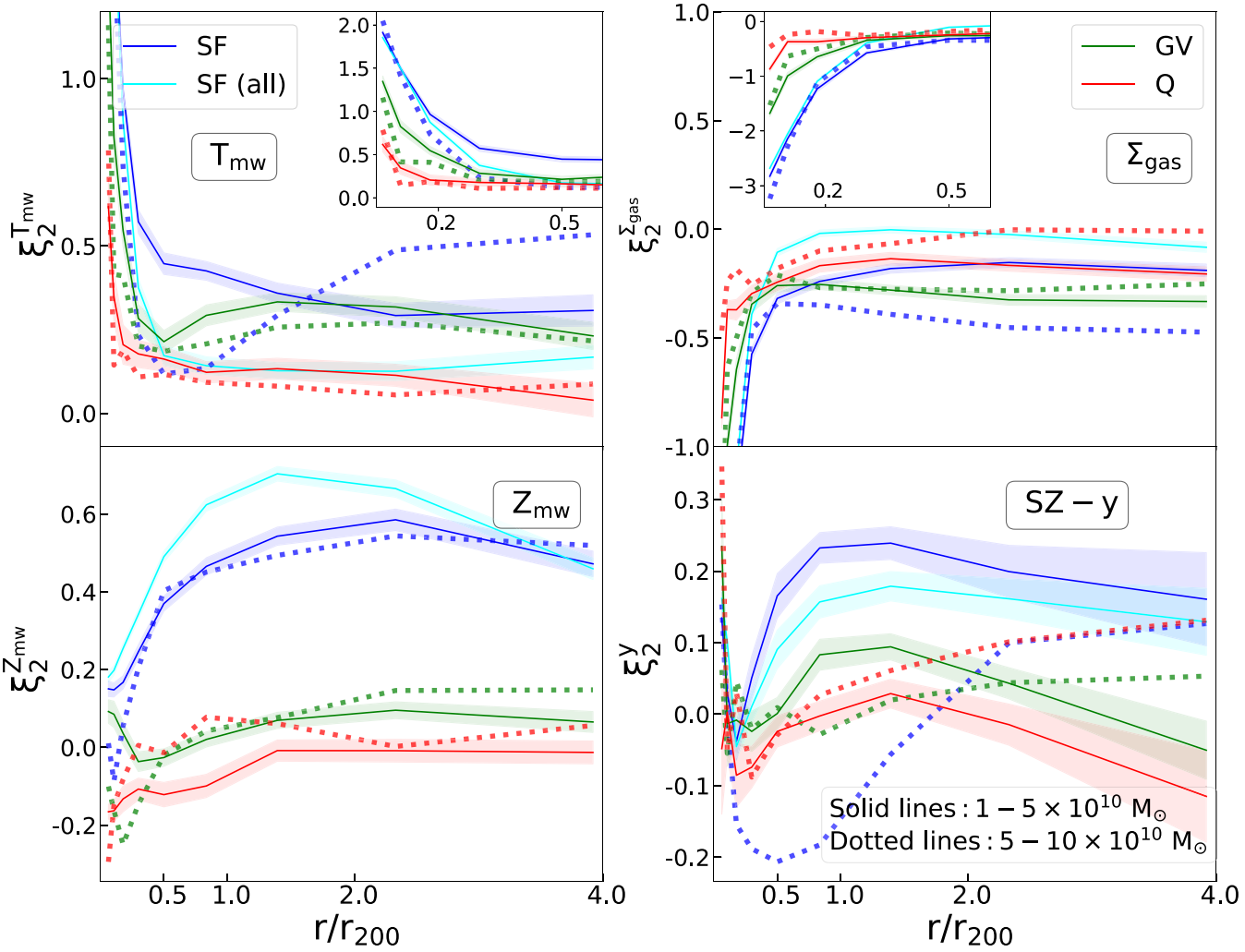

Figure 3. Comparison of mass-weighted gas temperature (T_{mw}), gas column density (Σ_{gas}), mass-weighted gas metallicity (Z_{mw}), and thermal SZ−y (y) quadrupole curves for different galaxy types (SF: blue, GV: green, Q: red), as a function of projected galactocentric distance. This aims to characterize the angular dependence of the CGM properties. Results are obtained for SIMBA -100 'jet-active' central galaxies at $z = 0.0$ within a low stellar mass bin ($M_* = (1–5) \times 10^{10}$ M$_\odot$, solid lines) and intermediate mass bin ($M_* = 5–10 \times 10^{10}M_\odot$, dotted lines). For comparison, results for all SF central galaxies with accretion rate > 0.0 within the lowest stellar mass bin are shown as cyan solid lines. Shaded regions show the bootstrap errors. For clarity, we omit the error regions around the curves obtained from the intermediate mass bin. In the top row, an inset within each panel zooms into the central region with $r \lesssim 0.5 r_{200c}$.

3.1 Dependence on galaxy type

Generally, galaxies start out with active star formation and evolve towards a red quiescent state, passing through the GV (Rodríguez Montero et al. 2019) – a phase where strong central suppression of star formation and lowered gas fractions are both clearly apparent (see Fig. 1; also Belfiore et al. 2018; Appleby et al. 2020). AGN feedback is believed to be a major source of energy for quenching galaxies. Recently, Cui et al. (2021) showed that jet feedback is the key mechanism that quenches galaxies in the SIMBA simulations. To connect with this picture, we first examine in this section how this evolution of star forming state and stellar mass imprints itself on the CGM anisotropy.

As discussed in Section 2.3, we subdivide the central galaxies into SF, GV, and Q samples selected from the SIMBA -100 fiducial run, and Fig. 1 indicates that strong AGN feedback mostly occurs within the stellar mass range 10^{10} M$_\odot \lesssim M_* \lesssim 10^{11}$ M$_\odot$, while massive galaxies with $M_* > 10^{11}$ M$_\odot$ show little feedback activity. Therefore, we only discuss results obtained from galaxies within a low-mass bin (with $M_* = (1–5) \times 10^{10}$ M$_\odot$) and an intermediate-mass bin (with $M_* = 5–10 \times 10^{10}$ M$_\odot$).

Fig. 3 shows the resulting mass-weighted gas temperature (T_{mw}), gas surface density (Σ_{gas}), mass-weighted gas metallicity (Z_{mw}), and thermal SZ−y (y) quadrupole measurements [computed using equation (5)] for SIMBA -100 'jet-active' central galaxies at $z = 0$ within low-mass and intermediate-mass bins. The shaded regions show the 1σ uncertainties in the quadrupole measurement determined by bootstrap resampling, as follows. For all projected galaxy maps measured from a given model, we construct a bootstrap catalogue by resampling galaxy maps with replacements but keeping the sample size the same as the original. These resampled maps are stacked as before, and the quadrupoles of each CGM property are directly measured on the normalized map. We then repeat this process 1000 times and compute the average as well as the standard deviation across the bootstrap samples.

By inspecting the T_{mw} (left-hand panel) and Σ_{gas} (second to left) curves obtained from the low-mass bin, it is clear that for SF galaxies

a gaseous disc feature is prominent in the central region, causing a negative quadrupole value at $r \lesssim 0.5r_{200c}$. This provides fuel to sustain star formation, although this lessens substantially going to GV and quenched systems. We will later show this quadrupolar enhancement is independent of feedback, so the anisotropy within $r \lesssim 0.5r_{200c}$ is not a test for feedback models.

At larger radii, however, we continue to see an enhancement of gas temperatures along the minor axis (jet direction) for SF and GV populations. We will later demonstrate that this is a signature of the large-scale impact of jets on the CGM. The cumulative effect of the jet remains powerful and significant up to the limit of this plot ($\sim 4r_{200c}$). For the SF case, the anisotropy falls at large distances, but it is still non-zero, indicating some residual effect from star-forming winds. For the GV case, ξ_T shows a dip and then increases slightly again at $r > r_{200c}$.

As a test, we applied the same analysis to SF galaxies without including any selection on jet activity. The resulting curves (shown as solid cyan lines) are mostly identical, except for the SF case in the low-mass bin. For these SF galaxies, the signature of the quadrupole is substantially reduced at $r > r_{200c}$, especially for the ξ_T curve, lying instead on top of the red Q curve. This indicates that the large-scale quadrupole seen in the SF case arises from selecting only those SF galaxies with ongoing jet activity. The GV curve remains unchanged because low-mass GV galaxies already tend to be jet active in the majority of cases.

An interesting situation occurs for SF galaxies in the intermediate mass bin (dotted blue curve). Here, there is a strong dip in ξ_T between $(0.5 - 1)r_{200c}$, even more prominent than for GV galaxies. This even persists when removing the active jet criterion, since at these higher masses even SF galaxies have active jets in most cases (see Fig. 1). By visually inspecting the edge-on projected map for these systems, we notice that a cavity is present along the minor axis, and a more isotropic hot gas distribution is formed around the central region, which suggests that the signatures of inflow are being strongly curtailed relative to lower-mass SF systems while the jet activity creates significant disturbances in the CGM at larger scales.

We now consider the $Z_{\rm mw}$ results (third panel in Fig. 3). One can see that a significant metal enrichment at large distances is measured in the SF samples, for both stellar mass bins considered in this study. As we will demonstrate later, this is primarily the consequence of active star formation, with some enhancement from strong jet feedback pushing metal-enriched gas out to large distances. For the GV and quenched cases, metallicity anisotropy features are much weaker, since their star formation rates and hence SF-driven winds are curtailed.

We now turn to the thermal pressure anisotropy around galaxies, as would be measured by the SZ y decrement (ξ_y, right-hand panel). The level of anisotropy here is much weaker than the anisotropy seen in other thermodynamic properties. This occurs because the thermal pressure is the product of gas temperature and density, and the latter two quantities have opposite angular dependences. This further suggests that the CGM of these galaxies rapidly equilibrate any pressure anisotropies introduced by non-spherical feedback. Unfortunately, it also suggests that SZ measures are not ideal probes of feedback-induced CGM anisotropy, unless combined with other measures that can disentangle the density and temperature. That said, in the star forming case the opposing trends of both curves do not completely cancel out, producing a slight but significant anisotropy in the thermal pressure at $r \gtrsim 0.5r_{200c}$.

In summary, our quadrupole analysis by galaxy SF activity indicates that at $r < 0.5r_{200c}$ there are large quadrupoles in temperature and surface density that correlate with SF activity. Beyond this, the quadrupole persists only when selecting jet-active galaxies, indicating that one must probe the small quadrupole at $r \gtrsim r_{200c}$ in order to test AGN feedback via CGM anisotropy. Despite these features, the y-decrement does not show strong anisotropy, indicating that the CGM rapidly isotropies any feedback-induced pressure variations. The metallicity anisotropy is strongest for SF galaxies, suggesting a connection to SF-driven outflows. In Section 3.3, we will flesh out these interpretations by examining how the quadrupoles depend on the physics that is included in the models. But next, we focus on exploring the mass dependence as a function of orientation angle.

3.2 Dependence on halo mass

In the previous section, we looked at the gas anisotropy for the two stellar mass bins where jet activity is seen, and focused on their connections to star-forming activity. Here, we explore the trends as a function of halo mass.

The top row in Fig. 4 shows the $T_{\rm mw}$, $\Sigma_{\rm gas}$, and $Z_{\rm mw}$ quadrupole radial profiles for the SIMBA -100 'jet-active' central galaxies within different stellar mass bins. We leave out the thermal SZ$-y$ feature due to its insignificant anisotropic levels compared to other CGM properties. Here, we include all samples with stellar mass $M_* \geq 10^{10}$ $\rm M_\odot$ and then further divide them into four bins.

The $T_{\rm mw}$ curves (upper left) show a significant change for $M_* > 10^{11}$ $\rm M_\odot$, below which the anisotropy shows a weak dependence on halo mass, while above this mass the quadrupole essentially disappears. More subtly, the dip in ξ_T at $\sim (0.5 - 1)r_{200c}$ is most prominent at (5–10) $\times 10^{10}$ $\rm M_\odot$, suggesting that the inflow signature is attenuating while the anisotropy induced by the cumulative effect of jets is increasing.

A similarly significant change is seen in ξ_Σ at $M_* > 10^{11}$ $\rm M_\odot$, above which the CGM gas suddenly becomes highly isotropic. The metallicity anisotropy shows a more complex behaviour, but again because quite low and even negative (i.e. aligned along the major axis) at high M_*.

As an alternative view of these trends, the bottom row of Fig. 4 presents the quadrupole values evaluated at three different galactocentric distances (shown in different colours) as a function of halo mass (with the approximately equivalent stellar mass shown along the top axis), for edge-on views. The radii are chosen beyond where the influence of anisotropic accretion is dominant ($r \geq r_{200c}$), to focus on the impact of AGN jet feedback.

For the edge-on case, the anisotropies of all three quantities are maximized at similar stellar mass ranges, with $\log_{10}(M_*/\rm M_\odot) \sim 10.5$–$11.0$ or $\log_{10}(M_{200c}/\rm M_\odot) \sim 12.2$–$12.5$. Combined with the strong amount of jet activity at lower masses ($M_* < 5 \times 10^{10}$ $\rm M_\odot$), this suggests that the net anisotropy at these larger radii is the result of the cumulative injection of bipolar feedback during the quenching process; subsequent to quenching being complete, this then rapidly becomes isotropized to leave no quadrupolar signature at the highest masses. We also performed an identical analysis for the face-on case, where the quadrupole values of all three quantities fluctuate around zero.

The 'turnover' at a transitional mass probably arises from an interplay between gas content and the modes of accretion and feedback. In the SIMBA fiducial runs, black hole seeds are placed in galaxies with $M_* \gtrsim 10^{9.5}\rm M_\odot$. Here, there is typically substantial cold gas within the inner disc region (as indicated by the $\xi_2^{\rm gas}$ curves), providing fuel for star formation, while the black holes accrete matter following the torque-limited model. At this stage, the black hole masses are still low: the Eddington ratios are high, so that no jet

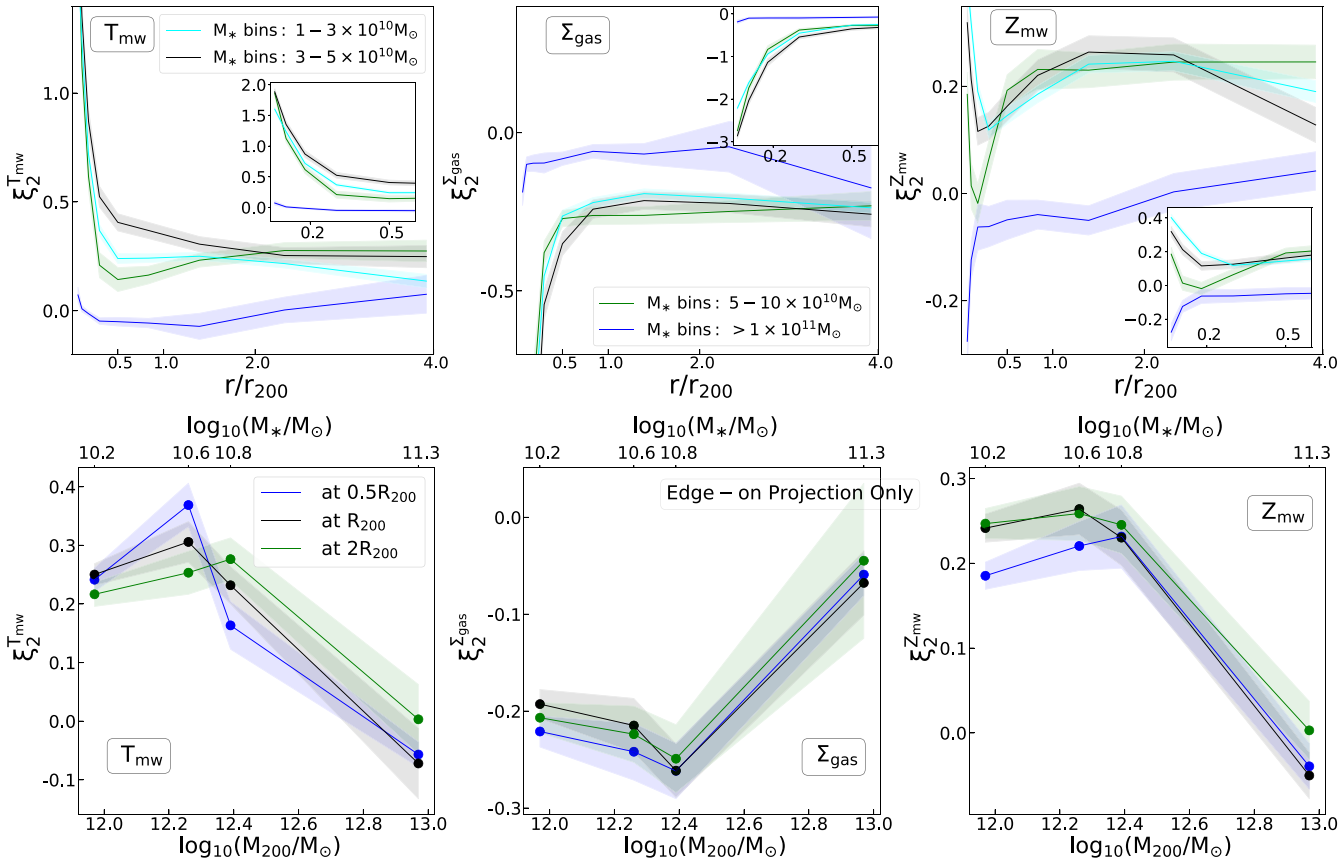

Figure 4. *Upper row*: mass-weighted temperature ($T_{\rm mw}$), gas column density ($\Sigma_{\rm gas}$), and metallicity ($Z_{\rm mw}$) quadrupole curves as a function of galactocentric distance for the SIMBA -100 'jet-active' galaxies at $z = 0.0$. This compares the results obtained from the edge-on projected maps within four stellar mass bins. Shaded regions show the bootstrap errors. In each panel, an inset zooms into the central region with $r \lesssim 0.5r_{200c}$. *Lower row*: quadrupole values for different CGM properties evaluated at various galactocentric distances. The symbols represent the galaxy-population stacked average within a given mass bin and the shaded regions show the bootstrap errors. Only the quadrupoles measured from the edge-on view are shown here for illustration. Halo masses and stellar masses are both labelled on the same plot for comparison. For SIMBA galaxies, the CGM presents the most significant anisotropic features at $\log_{10}(M_*/{\rm M}_\odot) \sim 10.5$–$11.0$ or $\log_{10}(M_{200c}/{\rm M}_\odot) \sim 12.2$–$12.5$.

activity is triggered. With the growth of central black holes (as well as their host galaxies), the Eddington ratio drops and the accretion transitions into Bondi mode; thus the feedback becomes dominated by jets. This explains why there are no jet-driven anisotropic signals at lower mass: it takes time for the BH to accumulate enough mass to have sufficiently low accretion rates that jet feedback can be initiated.

High-mass galaxies become quenched due to the accumulated AGN feedback from their progenitors. With no gaseous disc, the jet direction becomes more stochastic, because the black hole accretion region may lack a preferred angular momentum direction. We have found that jets in SIMBA vary in direction on time-scales of very roughly ∼100 Myr (Jennings, private communication), so this would isotropise the energy input over a long period. Furthermore, owing to the deep potential wells of such galaxies, their jets are more confined to the CGM. Those factors can all contribute towards creating a nearly isotropic CGM distribution around massive galaxies at larger scales.

Truong et al. (2021b) considered the same issue using IllustrisTNG central galaxies at $z = 0$. They found the mass-weighted temperature and gas density anisotropy to be peaked at $M_* \sim 10^{10.5\text{–}11}$ M$_\odot$, which is consistent with our findings. However, the distance dependence of our measured CGM anisotropy is much weaker than the TNG results: they found that, for low masses, the level of anisotropy depends significantly on the radius at which it is evaluated. Also, their metallicity anisotropy falls monotonically with galaxy mass, whereas our results suggest a turnover at a transitional mass range. These differences might arise from different methods for estimating the anisotropy, but are more likely to reflect the different subgrid physics adopted by the two simulations.

Overall, according to the quadrupole measurements, the anisotropy of $T_{\rm mw}$, $\Sigma_{\rm gas}$, and $Z_{\rm mw}$ are all maximized around the same stellar mass range, with $\log_{10}(M_*/{\rm M}_\odot) \sim 10.5$–$11.0$ or $\log_{10}(M_{200c}/{\rm M}_\odot) \sim 12.2$–$12.5$, with the anisotropy being weaker at lower masses and completely absent at higher masses. This result does not depend on the galactocentric radius. This peak in level of anisotropy at the transitional mass probably reflects the cumulative action of bipolar jets that causes galaxy quenching, with a rapid isotropisation together with a shutting off of inflow after quenching.

3.3 Dependence on SIMBA feedback models

We can most directly diagnose which feedback process is responsible for anisotropy at various scales and masses by looking at the SIMBA -50 variants, in which feedback mechanisms are shut off individually. We begin by visually inspecting the CGM distribution maps around SIMBA -50 galaxies evolved under different feedback models, and then quantify the differences using our quadrupole measure.

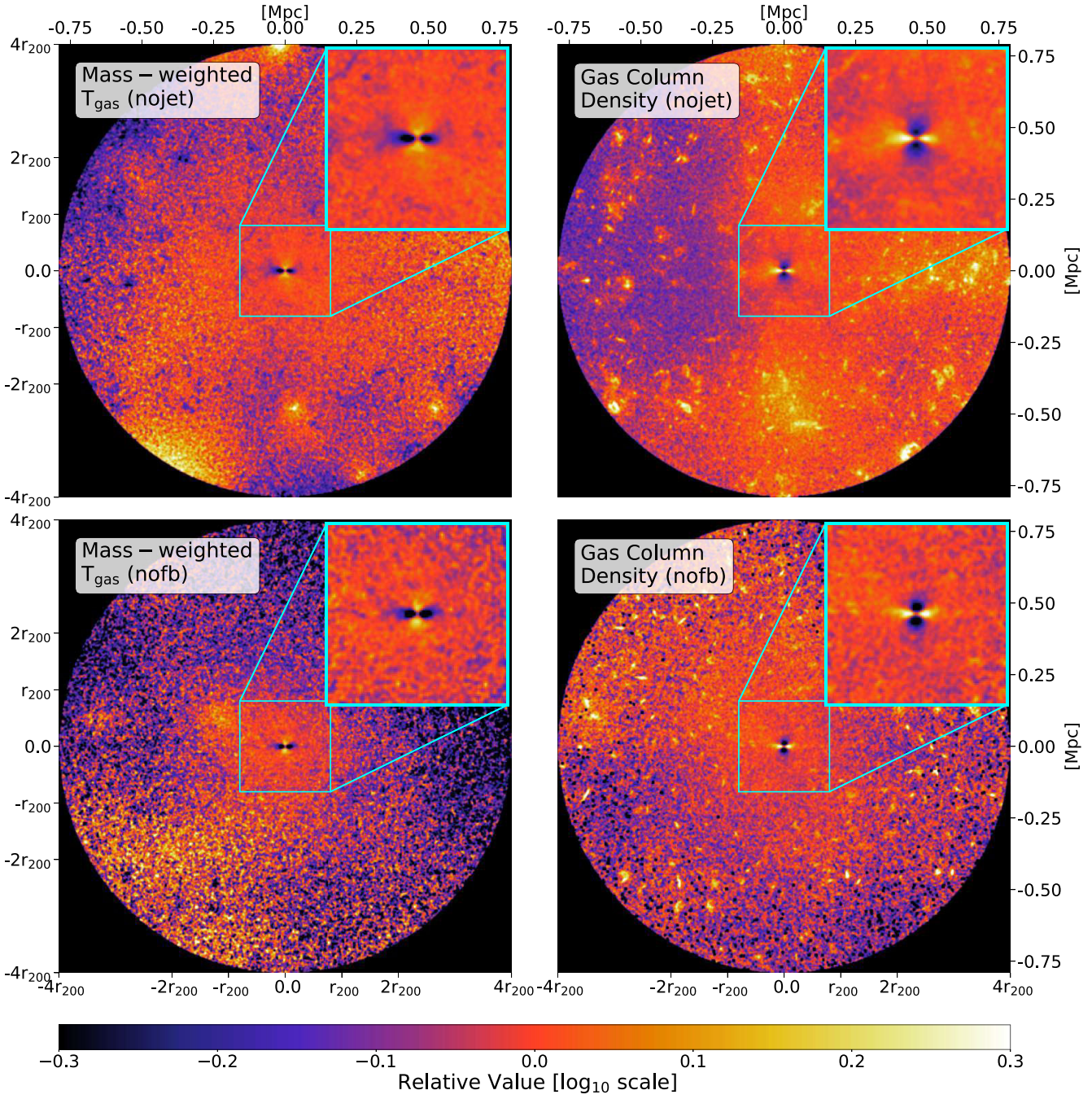

Figure 5. The same as Fig. 2 but here showing SIMBA -50-'nojet' (*top row*) and SIMBA -50-'nofb' (*bottom row*) model results for comparison. Host haloes across models are matched by their halo masses. The averaged halo mass is $\langle \log_{10}(M_{200c}) \rangle = 11.95$ for the SIMBA -50-'nojet' model and 11.90 for the SIMBA -50-'nofb' model.

In Fig. 2, we have already shown the edge-on stacked maps of CGM properties around central 'jet-active' galaxies selected from SIMBA -50-'allphys' at $z = 0$. For comparison, we conduct the same exercise but for central galaxies selected from the 'nojet' and 'nofb' run, where the former run has bipolar kinetic jet feedback plus X-ray heating turned off (top row), and the latter run has all simulated feedback activity turned off (bottom row). Host haloes across models are matched by using the dark matter particle IDs. The resulting stacked maps are showed in Fig. 5. In this case, we only show the stacked results for $T_{\rm mw}$ and $\Sigma_{\rm gas}$, because the anisotropic feature is not clearly seen in the y and $\Sigma_{\rm DM}$ 'allphys' maps.

By inspecting the differences presented in Figs 2 and 5, it is clear that around 'allphys' galaxies, owing to the jet activity, the gas temperature is significantly higher along the minor axis (jet direction), while conversely the gas density is extended along the major axis. After turning off the jet mode feedback (top row of Fig. 5), the strong large-scale bipolar anisotropy in the $T_{\rm mw}$ and $\Sigma_{\rm gas}$ maps disappears. Furthermore, due to the radiative AGN winds and star-forming winds still present in the 'no-jet' run, it is noticeable that the gas temperature is generally hotter and more extended around 'nojet' galaxies compared to those in 'nofb' (bottom row). In contrast, the small-scale anisotropy ($\lesssim 0.5 r_{200}$) in $T_{\rm mw}$ and $\Sigma_{\rm gas}$ remains present in

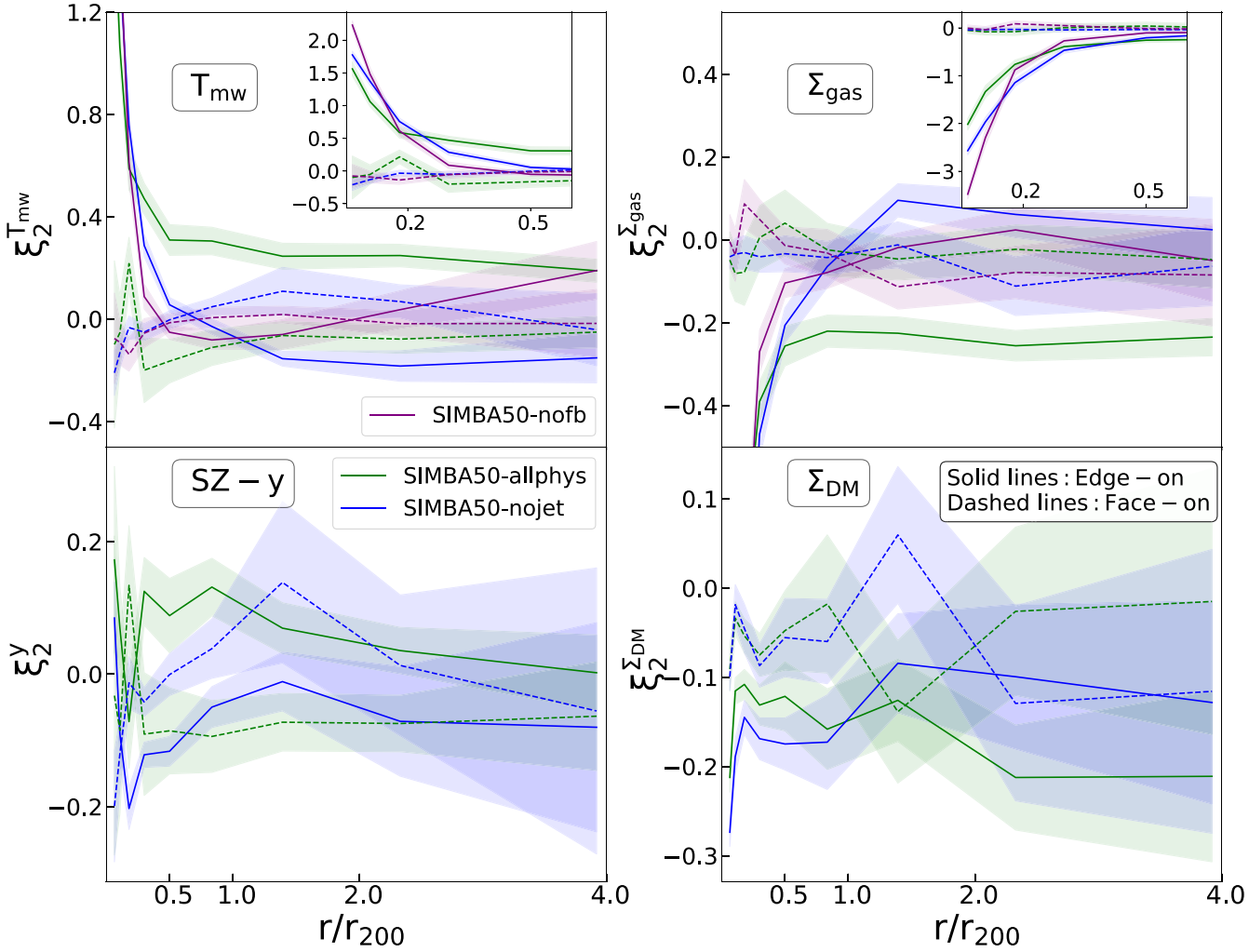

Figure 6. Quadrupole of mass-weighted temperature ($T_{\rm mw}$, *top left*), gas column density map ($\Sigma_{\rm gas}$, *top right*), the thermal SZ map (y, *bottom left*), and the dark matter column density map ($\Sigma_{\rm DM}$, *bottom right*), measured across SIMBA -50 model variants as a function of projected galactocentric distance. Results measured from both edge-on (solid lines) and face-on (dotted lines) projections are presented here. Shaded regions show the bootstrap errors. In the top row, an inset within each panel zooms into the central region with $r \lesssim 0.5r_{200c}$.

all runs, suggesting that it is a signature of cosmological gas accretion that is independent of feedback.

Fig. 6 presents the quadrupole results of different CGM properties as a function of projected galactocentric distance, measured from different AGN models (different coloured lines), which quantifies the trends seen in the projection maps. For reference, we also compute the quadrupole using a face-on projection (dashed lines), which as expected shows no anisotropy.

The quadrupole shows similar radial trends in the inner region ($r \lesssim 0.5r_{200}$) among all models. Hence the strong anisotropy within the inner halo is not a signature of feedback. To a certain degree, the inclusion of jet feedback suppresses the accretion on to the central black hole, causing a more elongated gas distribution along the major axis for models without jets. But given the strength of the intrinsic cosmological accretion quadrupole, it will probably be difficult to test any feedback-induced anisotropy within this regime.

At larger radii, it can be seen that our quadrupole calculation is more sensitive to different feedback models for the temperature and surface density. In particular, jet feedback generates higher temperature as well as a lower density region along the minor axis, and the cumulative jet effect still remains evident at distances $\gtrsim 4r_{200c}$. These features disappear when jets are off, as showed in the 'nojet' and 'nofb' case. This provides a 'sweet spot' for testing the AGN models in observations if using the CGM anisotropy.

The bottom panel of Fig. 6 presents the quadrupole measurement for thermal SZ$-y$ and $\Sigma_{\rm DM}$ from the 'allphys' and 'nojet' models. Unlike the strongly anisotropic features visible in $T_{\rm mw}$ and $\Sigma_{\rm gas}$, here the amplitudes of both quantities fluctuate around zero. As discussed previously, the opposing trends present in the gas temperature and density cancel out the anisotropic features in the thermal pressure (y). The relatively isotropic dark matter distribution (bottom right panel) on large scales indicates that the anisotropy of gas properties is not due to large-scale inflows/outflows of dynamical mass.

Moving on to the model dependence of $Z_{\rm mw}$ anisotropies. Fig. 7 shows the edge-on stacked $Z_{\rm mw}$ maps across SIMBA -50 models[1], and Fig. 8 shows the corresponding quadrupole measurements. We present the results obtained from all model variants because visual inspection showed that the CGM metallicity is the most sensitive

[1]Here, we omit the presentation of the 'nox' map because $Z_{\rm mw}$ anisotropies show similar trends in the 'nox' and the 'allphys' model.

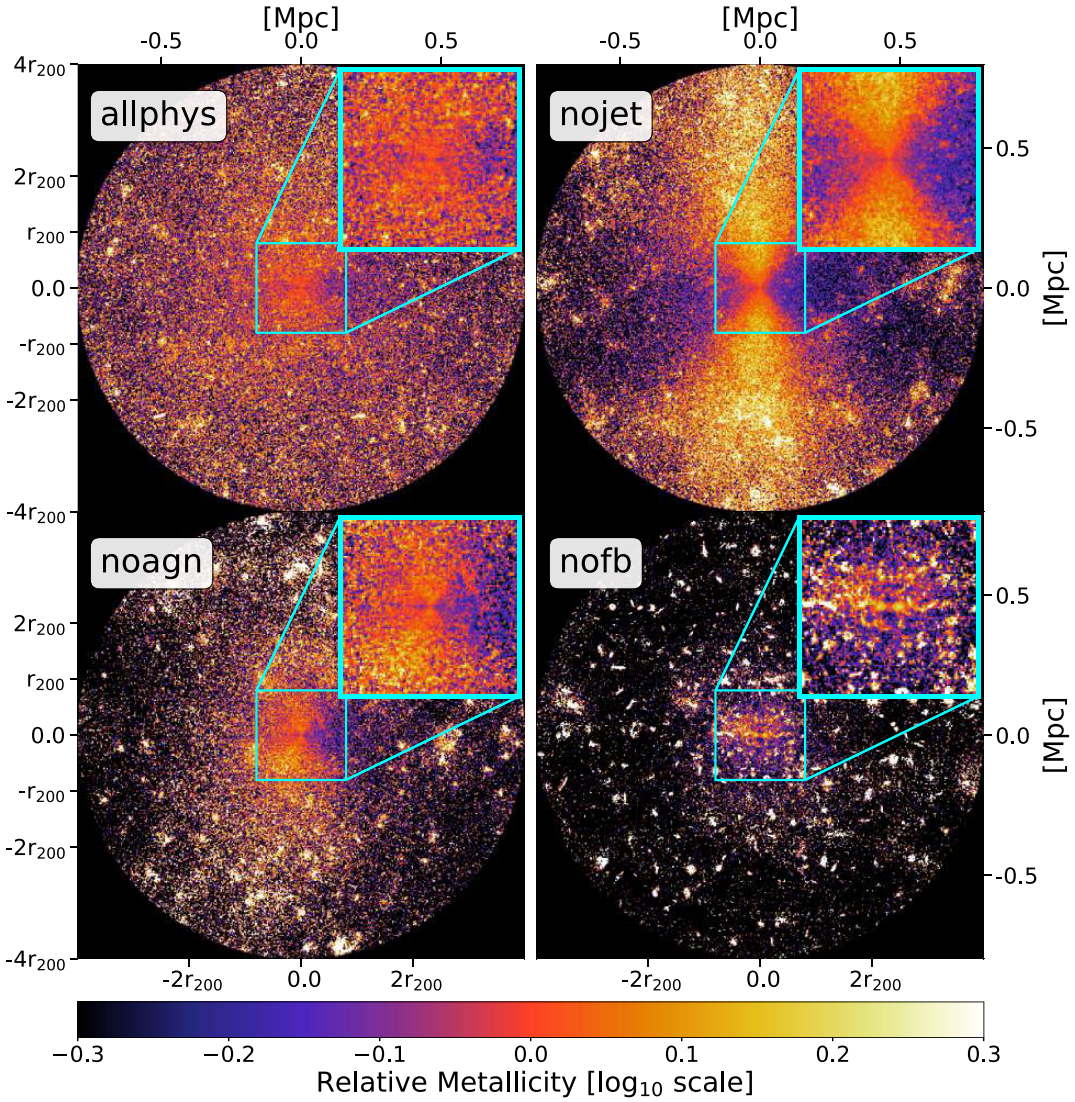

Figure 7. Anisotropy of the mass-weighted metallicity ($Z_{\rm mw}$) for 'jet-active' central galaxies at $z = 0.0$ in different SIMBA -50 models ($M_* = 1$–5×10^{10} M$_\odot$). Only the edge-on projection is shown. Maps are normalized with respect to the azimuthal average. Galaxies as well as their surrounding particle fields are rotated and stacked with the same approach as in Fig. 2. On each panel, the small window in the upper right corner zooms in to the central square region with a size of r_{200c}.

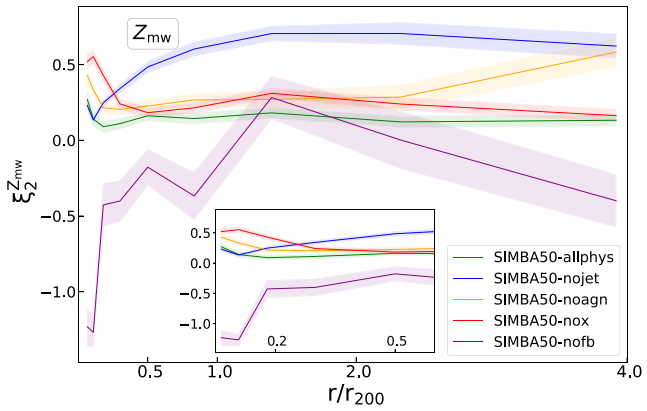

Figure 8. $Z_{\rm mw}$ quadrupole measurement as a function of galactocentric distance in different SIMBA models. For clarity, only results from the edge-on projection are shown. Shaded regions show the bootstrap errors. An inset panel zooms into the central region with $r \lesssim 0.5 r_{200c}$.

property to the feedback mechanisms. This might be expected because the resulting metallicity distribution in the CGM strongly depends on both star formation status and on the gas outflow models.

In the 'allphys' model, we do not see any significant anisotropic features around the galaxies: the measured quadrupole curve is fairly flat at all distances and only slightly above zero. This is primarily due to the curtailment of star formation and SF-driven winds in central galaxies, causing a weak metal enrichment of the CGM. As can be seen from Fig. 3, the metallicity anisotropy can be more prominent if a sample of galaxies with high star formation rate is selected, even with active jets turned on in their hosts. The 'nox' model shows similar results at larger radii, suggesting that the X-ray feedback is not the dominant factor for CGM metal anisotropy in this lowest stellar mass bin.

Interestingly, the 'nojet' model shows the most significant enhancement of metals along the minor axis. Compared to the 'allphys' case, the majority of 'nojet' populations have strong ongoing star-forming activity due to the lack of jets. Furthermore, as we shall see

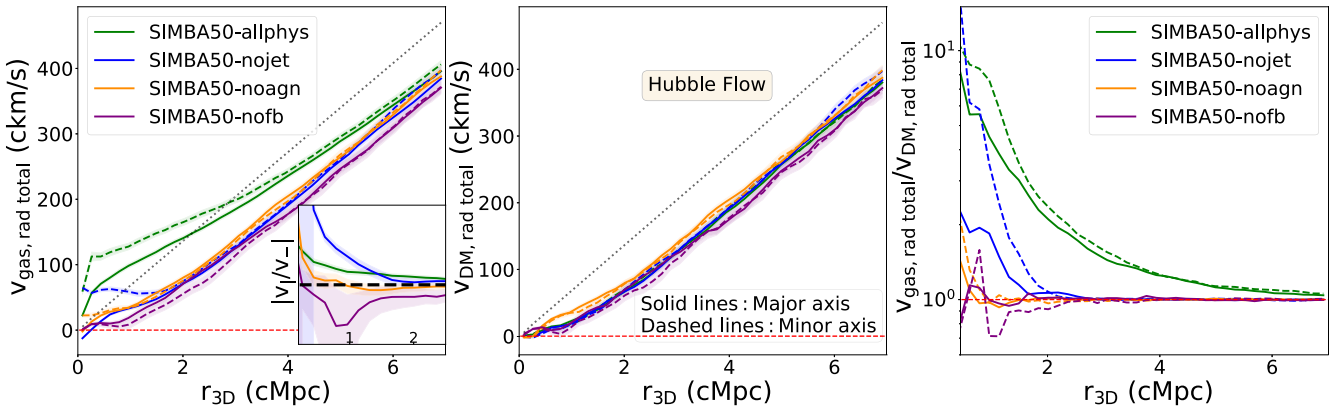

Figure 9. Total mass-weighted radial velocity for gas component (*left*) and dark matter component (*middle*) as a function of galactocentric distance in 3D, using 'jet-active' central galaxies with $M_* = (1-5) \times 10^{10}$ M$_\odot$ at $z = 0.0$. Measurements are performed within a 3D cone with an opening angle of $\pm 45^\circ$ around the axis. Dashed lines show the results from the cone aligned with minor axis, while the solid lines show the average curves from cones along the *X*-axis and the *Y*-axis on the galaxy major plane. In the left-hand panel, the ratio of quantities along the minor and major axes is shown as an inset in order to highlight the differences. Shaded regions represent the bootstrap errors. Models are distinguished by colours with the same colour scheme as in Fig. 7. Black dotted line: Hubble flow for comparison. To highlight the effective region of each AGN variants, the ratios between the gas and dark matter curves of each model are given in the *rightmost* panel for comparison.

below (Section 4.1, Fig. 9), the SF wind and radiative galactic outflow can carry gas out of the central star-forming regions up to $\sim$ 2 cMpc. This can effectively carry metal-rich gas out to $\sim 2r_{200c}$. The 'noagn' model shows weaker anisotropy because the stellar feedback is the only source that carries the metallic gas out, which is weak compared to AGN wind feedback. When all available feedback effects are turned off, metals can only be retained within galactic disks, as seen in the 'nofb' model. Therefore, although the star formation status of galaxies is the primary determining factor for their $Z_{\rm mw}$ anisotropy, how far the CGM can be enriched also depends on the power of AGN winds. In Section 4.1, we will investigate the wind power by exploring how the bulk radial gas motion depends on feedback models.

Because different studies used various tools to characterize the CGM anisotropy, it can be hard to make direct comparisons between them. Qualitatively, in agreement with the findings in the IllustrisTNG simulation (e.g. Nelson et al. 2019; Terrazas et al. 2020; Truong et al. 2021b), our quadrupole results suggest that the kinetic jet in SIMBA is powerful in reshaping the CGM properties and therefore regulating the star-forming activity of galaxies. As a consequence of jet feedback, gas accretion along the major axis can be prevented in the inner region. Meanwhile, gas particles can be heated and expelled out to a large galactocentric distance along the minor axis. However, the anisotropic features in $Z_{\rm mw}$ seen in our 'allphys' model are visually less prominent compared to the IllustrisTNG results (e.g. Péroux et al. 2020; Truong et al. 2021b), suggesting that some CGM properties are sensitive to the subgrid models adopted by different simulations. This is also apparent across SIMBA model variants (e.g. in Fig. 6).

To conclude, the angular dependence of the CGM is sensitive to the feedback models. The jet activity in the centre of a galaxy regulates its CGM on large scales, at $\sim 0.5r_{200c} - 4r_{200c}$ and beyond. The cumulative jet effect causes higher temperatures and lower densities along the galaxy minor axis (jet direction), in distinction to the isotropic distribution around samples where there is no jet. Due to the anisotropic accretion, the quadrupole moments show the strongest enhancement in the inner region ($r \lesssim 0.5r_{200c}$), but this feature is independent of feedback variants and therefore cannot be used for testing the feedback models. The CGM metallicity enrichment shows an complicated interplay between star formation activity and the effectiveness of feedback-driven winds, which will be examined in the next section.

4 FEEDBACK REGULATION OF GALAXY QUENCHING

The anisotropic distribution of the CGM presented in the previous section is a snapshot in time, but it should bear the cumulative imprint of feedback processes, and is connected to the properties of galaxies throughout cosmic time. In a way, it is a consequence of the interplay between CGM and galaxies. To understand how the the action of feedback take place, and how the anisotropy emerges throughout the evolution of the galaxies, we investigate the velocity field of the CGM in Section 4.1, and trace the properties of progenitor galaxies in Section 4.2.

4.1 Jet activity and radial outflows

To see the feedback process in action, we compare the radial velocity profiles of gas along the minor and major axes. To make an approximate separation between the jet direction and the disc direction, we consider gas particles around each galaxy within a 3D cone with an opening angle of $\pm 45^\circ$, and measure the average radial velocity profile within each shell of the cone using the following equation:

$$\overline{v}_{\,par,\,\mathrm{rad\,total}}(r_{\rm 3D}) = \sum_{i=0}^{N} m_{par,i} \left(\frac{\boldsymbol{v_i} \cdot \boldsymbol{r_i}}{|\boldsymbol{r_i}|} + H_0 |\boldsymbol{r_i}| \right) \Big/ \sum_{i=0}^{N} m_{par,i}, \quad (6)$$

where $\mathbf{v_i}$ is the relative peculiar velocity of a particle; $\mathbf{r_i}$ is its position vector relative to the black hole position; and m_i is the mass of a particle. The first term is the local peculiar velocity term and the second term accounts for the Hubble flow with $H_0 = 67.74\,\mathrm{km\,s^{-1}\,Mpc^{-1}}$. '*par*' stands for either non-star-forming gas or dark matter particles. The results are shown in Fig. 9.

We can see that the CGM radial velocities are mostly positive (left-hand panel), tending towards the Hubble flow at large scales, and reducing to nearly zero at small radii. This suggests that there is no gas

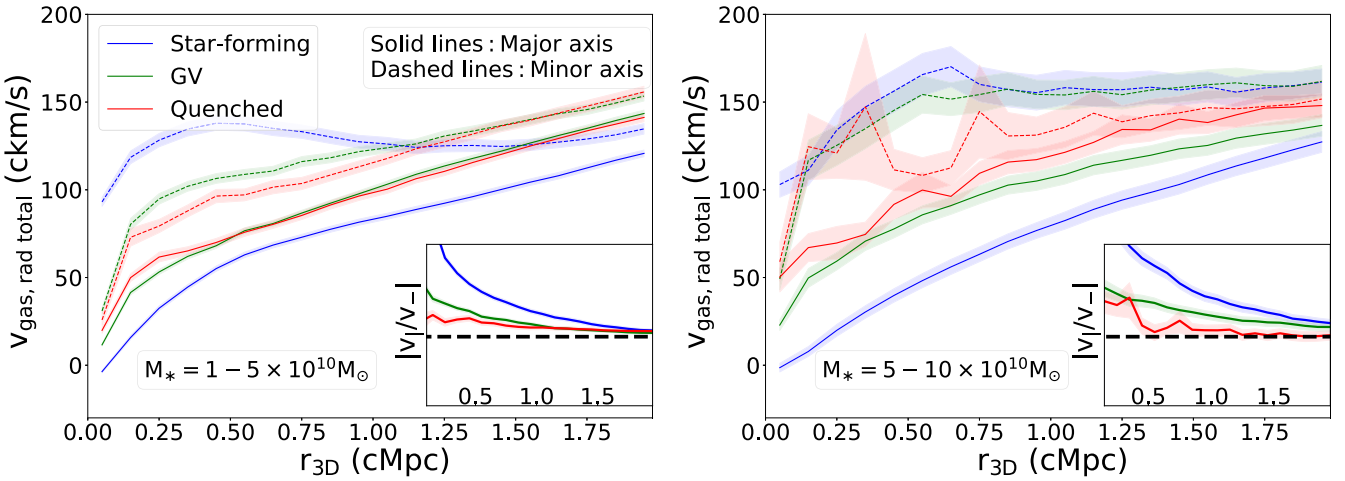

Figure 10. Gas total mass-weighted radial velocity as a function of galactocentric distance in 3D, using different types of 'jet-active' central galaxies at $z = 0.0$ within $M_* = (1\text{–}5) \times 10^{10}$ M$_\odot$ (*left*) and $M_* = 5\text{–}10 \times 10^{10}$ M$_\odot$ (*right*). Measurements are performed within the same cone regions as those for Fig. 9. Shaded regions represent the bootstrap error. Galaxy types are distinguished by colours, using the same colour scheme as in Fig. 3. In both panels, the ratio of quantities along the minor and major axes is shown as an inset in order to highlight the differences.

accretion for these galaxies on average. Their host haloes have also ceased to accrete dark matter, as seen in the middle panel. We do not expect dark matter to be directly influenced by feedback processes, and thus the phase-space curves of dark matter from different models are consistent with each other. They provide references for the CGM velocities, whose ratios to the dark matter version are shown in the right-hand panel. It is clear that the CGM in the 'allphys' and 'nojet' models shows a stronger outflow than the dark matter version. For the 'jet-active' central galaxies (green curves in the left-hand panel), the CGM outflow is much stronger than all other models. The outflow is even stronger along the minor axis (jet direction). This is evidence that jets are responsible for these strong outflows, which induce the large-scale CGM anisotropy we have seen in the previous section.

It is worth noting that for the 'nojet' model, there is also a sign of enhanced outflow within ~ 1.5 cMpc along the minor axis (blue-dashed curve on the left), but this is much less effective than jet-induced AGN feedback in carrying gas out to further distances.

These results support the physical picture that, along the minor axis, kinetic jet feedback is the most powerful driver in expelling hot gas out to large scales ($\sim 3-4$ cMpc). Additionally, radiative AGN winds are also capable of carrying gas out to $\sim 1-2$ cMpc, but the radiative mode alone is not able to suppress the star formation activity and the chemical enrichment due to stellar feedback. This explains the strong large-scale metallicity enrichment seen for the 'nojet' case in Fig. 7. The effect of stellar feedback may have a minor impact within $r_{3D} \lesssim 1$ cMpc, but it is much weaker compared to the AGN winds. In general, bipolar kinetic jet feedback drives gas ejection and heating out to large distances, prevents gas cooling in the central star-forming region. We conclude that the combination of both these 'ejective' and 'preventative' modes is essential for the effective quenching of SIMBA galaxies.

When splitting the sample into SF, GV, and Q populations, we find that the SF galaxies have the strongest outflows along the minor axis at small radii, followed by GV and Q galaxies (Fig. 10). Moreover, the difference in the strength of the outflow between the minor (dashed lines) and major axes (solid lines) decreases across the three types of galaxies. This again suggests a strong correlation between jet activity and galaxy type. In addition, there may be signs of thermalisation of the energy carried out by jets. A possible scenario is that jets in SF galaxies initially carry kinetic energy out along the minor axis and the energy thermalises the CGM as they travel, increasing the CGM temperature and boosting the outflow along the minor axis. These processes gradually quench star formation, causing the galaxies to evolve from SF into GV, and eventually Q. A supporting argument for this picture is that on the left-hand panel the blue-dashed curve is the highest at small radii ($r_{3D} < 1.2$ cMpc), but the green- and red-dashed curves take over at larger radii. It is possible that we are seeing the jet energy propagating outwards from the galactic centres, gradually increasing the outflow velocity at large radii while causing the galaxies to evolve to be GV and Q.

Table 2. Redshift evolution of the galaxy types for progenitor-descendant galaxy pairs. The numbers of 'jet-active' galaxies within each galaxy type are shown in the brackets.

Redshift	SF	GV	Q	Total
$z = 1.0$	218 (33)	130 (124)	25 (24)	373 (181)
$z = 0.5$	34 (27)	249 (247)	90 (90)	373 (364)
$z = 0.0$	0 (0)	0 (0)	373 (373)	373 (373)

4.2 Redshift evolution of feedback activity

The possible scenario of galaxy evolution from SF to GV and to Q regulated by feedback processes is best examined by tracing the evolution of galaxies directly in our simulations. To do this, we identify the progenitors of a sample of quenched galaxies with $M_* = (1\text{–}5) \times 10^{10}$ M$_\odot$ at $z = 0$.

We identify progenitors by finding galaxies at a high redshift that have the most stellar particles in common with those at $z = 0$. We make extra cuts in accretion rate and stellar mass such that galaxies at higher redshifts have accretion rate > 0 and have stellar mass within the range identical to those at $z = 0$. We do not select the progenitors to be 'jet-active', in order to include the cumulative effect of all possible feedback mechanisms at higher redshifts. Results at $z = 1$, 0.5, and 0 are presented in Table 2 and Fig. 11.

By default, galaxies selected at $z = 0.0$ are all 'jet-active' quenched members. As shown in this table, their progenitors at $z = 1$ are mainly star-forming galaxies, with a fraction of them being jet-active, i.e.

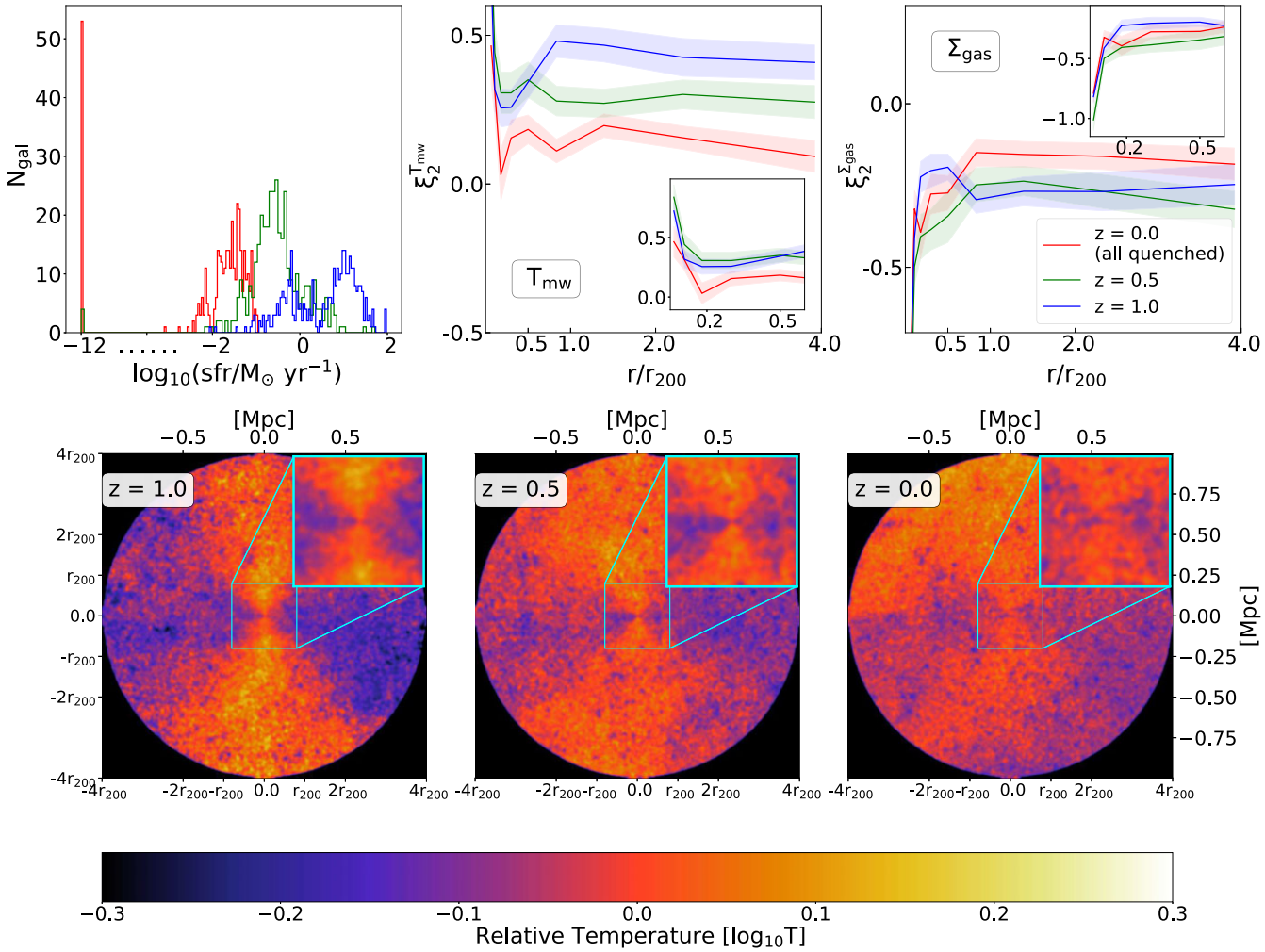

Figure 11. Redshift evolution of feedback activity. Progenitors are traced back to $z = 1.0$ for $M_* = (1\text{–}5) \times 10^{10}$ $M_\odot$ quenched galaxies at $z = 0.0$, where progenitors are defined as having the most stellar particles in common. A one-to-one matching is performed within the same stellar mass range with accretion rate > 0 across snapshots. *Top*: the histogram of star formation rate evolved with redshifts and the redshift evolution of $T_{\rm mw}$, $\Sigma_{\rm gas}$ quadrupole curves as a function of galactocentric distance. Only results from $z = 0.0$ (red solid), 0.5 (green solid), and 1.0 (blue solid) are shown here for illustration. An inset within each panel zooms into the central region with $r \lesssim 0.5 r_{200c}$. *Bottom*: The edge-on $T_{\rm mw}$ stacked maps at different redshifts for visual inspection. It is clear that the progenitors of quenched galaxies undergo stronger AGN feedback at earlier times.

they have achieved the full jet speed. Note that the majority of the remaining galaxies at $z = 1$ still have jet activity, but their jets have not reached full speed. Most of these galaxies evolve into GV by $z = 0.5$, and become jet-active. By $z = 0$, all of them are quenched, and remain jet-active. This is also illustrated on the top-left panel of Fig. 11, where the continued decline of star-forming population with redshift is evident.

The $T_{\rm mw}$ and $\Sigma_{\rm gas}$ quadrupoles, measured at different redshifts, are shown in the middle and right top panel. For reference, the edge-on stacked $T_{\rm mw}$ maps at three redshifts are presented in the bottom row. Based on the $T_{\rm mw}$ quadrupole, an 'ejective' effect from feedback at high redshift is clearly seen at outer region. Combining with the $T_{\rm mw}$ map given in the bottom row, one can see that those high-z progenitors were undergoing strong bipolar AGN feedback at earlier times. Owing to this, gas particles were heated and ejected from the central star-forming region. Hot gas then accumulated in the CGM and eventually thermalised in the outer regions, until the time when the hot gas is isotropically distributed around the central galaxies and the fuel for further star formation is depleted. Then jets are responsible for maintaining the galaxies in a quenched state at $z = 0.0$.

At face value, there is a correlation between star formation rate with the level of CGM anisotropy on large scales across different redshifts, i.e. as the population evolves from being star-forming at high redshift to being quenched at low redshift (Table 2), the level of CGM temperature anisotropy also decreases (middle panel of Fig. 11). It is not immediately clear whether it is star formation or AGN jets that are responsible for the anisotropy. To test this, we repeat our stacking analysis with a sample of galaxies at $z = 1$ that have no jet activity at all, but still with star formation and radiative feedback. Results are presented in Fig. 12. It is clear that the CGM for this sample is anisotropic, but the feature is present at relatively small scales, confined to be within $1 - 2r_{200}$. Based on this, we conclude that while other feedback processes can contribute to the CGM anisotropy on small scales, jet activity should be responsible for it on large scales. This is a distinct feature for the jet model that may provide observational signatures for detecting the direct impact of the jets on the CGM,

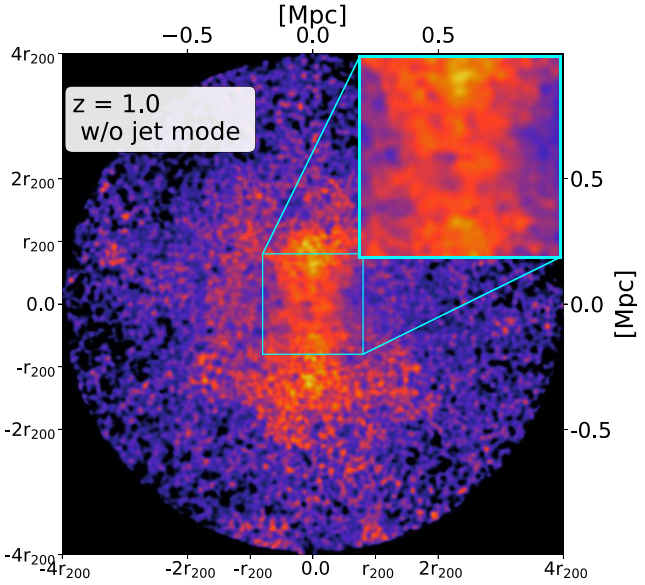

Figure 12. The edge-on $T_{\rm mw}$ stacked maps for $z = 1.0$ progenitors without kinetic-jet mode. It is clear that the star formation and radiative feedback alone are not strong enough to expel gas out to large distances.

and being able to tell the jet model apart from other feedback mechanisms.

In general, this supports the picture that strong AGN feedback plays a crucial role in effectively suppressing the star formation and maintaining the galaxies in the 'quenched' state at $z \leq 1$. This once again demonstrates the strength of the SIMBA AGN feedback model: the feedback winds are capable of ejecting and heating up the gas to a large distance ('ejective' effect). As shown by Sorini et al. (2022), the SIMBA AGN-jet feedback mode can displace baryons out to $\sim 4\,r_{200c}$ at $z < 1$ and even $\sim 10\,r_{200c}$ at $z = 0$, and increases the amount of hot gas in the outskirts of the halo. On relatively small scales, this process is further helped by star formation and radiative feedback. Hot gas accumulates in the CGM and then thermalizes around central galaxies, which prevents the gas from cooling and falling back on to the inner star-forming region ('preventative' effect). This gas starvation drives galaxy quenching and the jet further maintains the quenched state at low redshift. This also explains the relatively lower level of CGM anisotropy for quenched galaxies at $z = 0$ shown in Fig. 3.

5 COMPARISONS TO OTHER SIMULATIONS

The anisotropic distribution of CGM is not unique to SIMBA . In fact other models with AGN feedback, such as the kinetic one adopted by the TNG100 simulation and the thermal one from the EAGLE simulation may also predict CGM anisotropy (Truong et al. 2021b; Nica et al. 2022; Truong et al. 2023), but existing studies have not covered a range of scales as large as the one explored here (see also Fig. 12).

Truong et al. (2021b) carried out analyses of the TNG100 simulation that are qualitatively similar to ours; instead of using the quadrupole, the level of CGM anisotropy in their work was characterized by the minor-to-major axis ratio. The angular dependence displayed on their median stacked CGM maps, around central galaxies with $M_* = 10^{11 \pm 0.1}{\rm M}_\odot$ from TNG100 at $z = 0.0$, are qualitatively similar to our results: an underdense region of CGM gas along the minor axis with an enhancement of temperature and metallicity, even though the direction of jets is randomised at each time-step in the TNG model. In addition, the levels of anisotropy in $T_{\rm mw}$ and $\Sigma_{\rm gas}$ are also maximized at a transitional mass range with $M_* \sim 10^{10.5-11}{\rm M}_\odot$ ($M_{200c} \sim 10^{12.1-12.5}{\rm M}_\odot$). These are consistent with our findings shown in Fig. 4.

However, there are some noticeable differences between the study with TNG and our results from the 'allphys' models, including (i) a more prominent metallicity ($Z_{\rm mw}$) anisotropy along the minor axis in TNG, and features in that study that monotonically decrease with galaxy masses; (ii) a stronger dependence on the galactocentric distance in TNG when evaluating the level of CGM anisotropy, especially for galaxies with $M_* \lesssim 10^8$ M$_\odot$ ($M_{200c} \lesssim 10^{12.5}$ M$_\odot$); (iii) stronger anisotropic features in $T_{\rm mw}$ and $\Sigma_{\rm gas}$ for massive galaxies in TNG that are quenched and non-discy compared to their star-forming counterparts.

Nica et al. (2022) used mock eROSITA-observations from the EAGLE simulation to study the azimuthal dependence of CGM X-ray emission. They found that the anisotropic features strongly depend on the galaxy morphology: for spheroids, the CGM distribution tends to be more isotropic, while for disc galaxies, there are clear bipolar outflows along the minor axis driven by feedback, especially seen in the stacked temperature and metallicity maps. These are consistent to our findings here in the SIMBA model. However, their X-ray results do not show strong bi-conical features around the disc-like population. Instead, the emission is more extended along the major axes. This is because the strength of feedback-driven hot gas outflows are much weaker than the density enhancement along the discs. In terms of CGM anisotropy, Truong et al. (2021b) made a comparison between the TNG and EAGLE simulations: although the two simulations predict similar CGM geometries, they produce different mass dependences: especially at low mass ($M_{200c} \sim 10^{11.5}$ M$_\odot$), the bipolar gas outflows around TNG galaxies are much stronger compared to those from EAGLE (see their Fig. 6).

These differences in CGM properties are not surprising, given the different feedback models implemented in the simulations. As discussed in Truong et al. (2021b), the resulting CGM anisotropy around TNG, Illustris, and EAGLE galaxies can be significantly affected by the detailed stellar and AGN feedback mechanisms. Also, previous tSZ−y studies (e.g. in Yang et al. 2022) have shown that, compared to the TNG model, the adopted SIMBA feedback model is more energetic at heating and expelling gas into the CGM. Therefore, gas in the CGM can be thermalised more efficiently around galaxies, producing a more isotropic hot gas distribution around massive quenched galaxies compared to those in the TNG simulation. This could explain why the anisotropy levels around SIMBA quenched galaxies are lower that those seen in TNG. Meanwhile, the strong suppression of star formation owing to the powerful feedback causes the depletion of metal-enriched gas in the central region. As seen in Fig. 3, the level of $Z_{\rm mw}$ anisotropy can be much more prominent compared to the GV and Q counterparts. Beyond that, it is worth nothing that the CGM anisotropic signals along the major axes can also be driven by non-feedback inflows, as discussed by some simulation studies (for further details, see e.g. Hafen et al. 2022; Stern et al. 2023).

6 IMPLICATIONS FOR OBSERVATIONS

We have used the SIMBA model to show that jet activity from AGN can provide powerful energy feedback, which regulates star-forming activity for the galaxy, and leaves imprints on the properties of the CGM. This opens possibilities for constraining feedback models with observational signatures of the CGM. It has been shown

that the CGM properties around galaxies, such as the azimuthal asymmetry and the X-ray projected profile, have a large dependence on the adopted feedback models. Based on the mock observations from TNG, EAGLE, and SIMBA simulations, recent studies have shown the potential ability of detecting these differences in more detail using future X-ray microcalorimeters (Ayromlou, Nelson & Pillepich 2023; Schellenberger et al. 2023; Truong et al. 2023), e.g. from Line Emission Mapper (LEM; Kraft et al. 2022). In fact, by stacking galaxies from the state-of-the-art X-ray observations (e.g. from eROSITA: Predehl et al. 2021), the CGM properties, such as the projected luminosity and radial profiles have already presented clear differences around different types of galaxies (Chadayammuri et al. 2022; Comparat et al. 2022). These observations, however, show some discrepancies with simulated results, which may indicate imperfections in the current feedback models.

In terms of the CGM anisotropy, one key step in being able to identify the direction of the jet for the stacking of the CGM, which can be challenging in practice. However, one can use other observable means to infer the jet directions. The stellar disc is an observable that may correlate with the jet direction due to the expected alignment of the angular momentum of the centre of a disc galaxy with that of the stellar disc, or even with the HI gas. We have explicitly studied the angular momentum of the BH and stellar disc from the SIMBA simulations, and confirmed that there is a strong, though not perfect, correlation between them. This is further evident from the results presented in Fig. A1, where we repeat our analyses for the anisotropy of the CGM, but instead of using the jet directions, we use the stellar angular momentum vectors as proxies. We see that the results remains similar. Therefore, at least in SIMBA simulations, the direction of the stellar angular momentum is a good approximation for the jet direction. This provides one possible guide for future observational analyses of this kind.

From both observations and simulations, the satellite quenching fraction is found to be anisotropically distributed around the central hosts, where a larger quenching fraction is found along the minor axis compared to that within the major plane (e.g. in Zaritsky et al. 1997; Martín-Navarro et al. 2021). Also, previous studies have shown that the spin vectors of high-mass haloes and galaxies (with $M_{\rm halo} \gtrsim 10^{12}$ $h^{-1}{\rm M}_{\odot}$) are on average perpendicular to the filament axes (e.g. in Ganeshaiah Veena et al. 2018, 2019). This provides us with some possible indirect means of linking the direction of galactic outflow with large-scale accretion flows.

Once the jet direction is found, the large-scale CGM anisotropy in temperature and gas density is a clear signature that can be sought in observational data. It is also clearly distinct from the relatively small-scale features induced by other feedback processes (Truong et al. 2021b). We have shown that the thermal SZ effect, which is sensitive to the gas pressure, is probably not a good observable for this because the anisotropy shown in the SZ-y maps is weak due to the cancelling effect between an increased gas temperature and a decreased gas density. However, the X-ray emission is sensitive to the square of the gas density, and only weakly on the gas temperature. This is different from that of the tSZ signature. The combination of X-ray data with tSZ measurements may allow us to measure the temperature map of the CGM (e.g. Adam et al. 2017).

Furthermore, the most anisotropic direction or jet direction can be directly determined using observational data, such as from X-ray and radio surveys. The current state-of-the-art X-ray missions, *Chandra* and *XMM–Newton* (Giles et al. 2016; Luo et al. 2017), have already revealed giant cavities and hot gas shock fronts along the minor axes of massive galaxies (e.g. Hlavacek-Larrondo et al. 2015; Liu et al. 2019). Specifically, new generation X-ray surveys such as *eROSITA* are capable of sampling millions of AGN by scanning the whole sky within a much wider range of energies (0.2-10 keV: Predehl et al. 2021). Truong et al. (2021b) have demonstrated that the predicted X-ray hardness from an *eROSITA*-like survey can be helpful and promising for capturing bipolar CGM features, and this property is quite sensitive to the adopted feedback models in simulations. However, one needs to stack a large number of samples ($\gtrsim 10^4$) to reach an SNR greater than 3 around halo mass $M_{200c} \sim 10^{12}{\rm M}_{\odot}$. The all-sky coverage of *eROSITA* allows the stacking of large samples and allows us to conduct anisotropy analyses of the thermodynamic gas properties in the CGM. For AGN possessing collimated radio jets, telescopes such as the *VLA* and *LOFAR* have good sensitivity to extended sources (Baldi, Capetti & Massaro 2018; Croston et al. 2019). As suggested by our results, the accumulated CGM anisotropy features from powerful jet feedback should still be significant up to several Mpc. The advent of these surveys will enable the investigation of feedback-induced CGM anisotropy out to larger radii.

7 CONCLUSIONS AND DISCUSSION

We have used SIMBA simulation model variants to explore how the properties of galaxies and their CGM are regulated by feedback processes, with a focus on the jet activity of their central black holes. We find that at redshift $z < 1$, central galaxies with active AGN jet feedback are most commonly found in the stellar mass range between (1–5) $\times$ 10^{10} ${\rm M}_{\odot}$, and most commonly within the green valley (Fig. 1). Driven by the powerful bipolar jet-activity, the CGM becomes anisotropic in temperature, gas density, and metallicity at the galactocentric distance of $4r_{200}$ and beyond. This is supported by direct evidence from the outflow of the gas extended to several cMpc, and that the outflow is stronger along the jet direction. We have also show evidence that jet activity is responsible for driving the galaxy to evolve from being star forming to occupying the green valley, and eventually moving into a quenched state.

On large scales ($r > 0.5r_{200}$), the jets increase the gas temperature around the minor axis of a galaxy while suppressing its density. These features are similar to those seen in star formation and radiative feedback processes, but the latter occurs at relatively small scales ($r < 2r_{200}$). The difference in the scale of impact on the CGM is potentially a unique signature for distinguishing the jet model from other type of feedback processes. Due to the cancellation effect, the resultant gas pressure remains relatively isotropic. This makes it challenging to use the thermal SZ effect alone to detect the effect of the jets on the CGM, but it may be possible with the combination of SZ and X-ray observables.

The CGM metallicity is strongly enhanced along the minor axis around SF galaxies, peaking at around r_{200}. This disappears for GV galaxies, and Q galaxies even show a slight metallicity enhancement along the major axis. Given that star formation is the expected source for metal enrichment, it is likely that star formation provides the metals, which are then carried out by the jets to larger scales. We do not find any obvious anisotropy for the dark matter, as expected.

On small scales ($r < 0.5r_{200}$) we also find strong anisotropy for the CGM, but this is common to different feedback models, even when all explicit feedback is turned off, indicating that it is associated with anisotropic cosmological accretion rather than any feedback process.

Understanding how feedback activity regulates the baryonic cycle is a crucial step in galaxy formation and evolution. From the above analysis, it is apparent that the CGM anisotropic features depend strongly on the feedback models, and it is a consequence of both 'ejective' and 'preventative' effects that leave an imprint on the resulting CGM properties. The SIMBA 'allphys' simulation and its

model variants provide us an ideal opportunity to compare and predict what may happen around galaxies selected from different environments. By observing the CGM distribution, one can further infer the host galaxy properties, such as the star formation status and the impact of feedback.

While this study has focused on theoretical aspects, we hope to provide inspiration and observational directions for future CGM studies, such as from which direction one expects to observe the strongest CGM anisotropy signal. Apart from the central region, the accumulated effect of feedback activity around low-z galaxies can be 'observed' out to several Mpc, so there are good prospects of making the necessary measurements in practice. With the advent of new surveys and improved simulation models, these probes of anisotropic CGM properties should enable us to learn ever more about the detailed operation of feedback in galaxy formation.

ACKNOWLEDGEMENTS

We are grateful for the publicly available simulations from the SIMBA project. During this work, DS and JAP were supported by the STFC consolidated grant no. RA5496. DS was further supported by the Swiss National Science Foundation (SNSF) Professorship grant no. 202671. WC is supported by the STFC AGP Grant ST/V000594/1 and the Atracción de Talento Contract no. 2020-T1/TIC-19882 granted by the Comunidad de Madrid in Spain. He also thanks the Ministerio de Ciencia e Innovación (Spain) for financial support under Project grant PID2021-122603NB-C21 and ERC: HORIZON-TMA-MSCA-SE for supporting the LACEGAL-III project with grant number 101086388. RD acknowledges support from the Wolfson Research Merit Award program of the U.K. Royal Society. YC acknowledges the support of the Royal Society through a University Research Fellowship and an Enhancement Award. This work used the DiRAC@Durham facility managed by the Institute for Computational Cosmology on behalf of the STFC DiRAC HPC Facility. The equipment was funded by BEIS capital funding via STFC capital grants ST/P002293/1, ST/R002371/1, and ST/S002502/1, Durham University and STFC operations grant ST/R000832/1. DiRAC is part of the National e-Infrastructure.

DATA AVAILABILITY

The raw SIMBA simulation data and halo catalogues used in this paper are available at https://simba.roe.ac.uk. The remaining data will be made available on request to the lead author.

REFERENCES

Adam R. et al., 2017, A&A, 606, A64
Anglés-Alcázar D., Özel F., Davé R., Katz N., Kollmeier J. A., Oppenheimer B. D., 2015, ApJ, 800, 127
Anglés-Alcázar D., Davé R., Faucher-Giguère C.-A., Özel F., Hopkins P. F., 2017a, MNRAS, 464, 2840
Anglés-Alcázar D., Faucher-Giguère C.-A., Kereš D., Hopkins P. F., Quataert E., Murray N., 2017b, MNRAS, 470, 4698
Appleby S., Davé R., Kraljic K., Anglés-Alcázar D., Narayanan D., 2020, MNRAS, 494, 6053
Appleby S., Davé R., Sorini D., Storey-Fisher K., Smith B., 2021, MNRAS, 507, 2383
Appleby S., Davé R., Sorini D., Cui W., Christiansen J., 2023, MNRAS, 519, 5514
Ayromlou M., Nelson D., Pillepich A., 2023, MNRAS, 524, 5391
Baldi R. D., Capetti A., Massaro F., 2018, A&A, 609, A1
Belfiore F. et al., 2018, MNRAS, 477, 3014
Bondi H., 1952, MNRAS, 112, 195
Bordoloi R. et al., 2011, ApJ, 743, 10
Bouché N., Hohensee W., Vargas R., Kacprzak G. G., Martin C. L., Cooke J., Churchill C. W., 2012, MNRAS, 426, 801
Bouché N., Murphy M. T., Kacprzak G. G., Péroux C., Contini T., Martin C. L., Dessauges-Zavadsky M., 2013, Science, 341, 50
Chadayammuri U., Bogdán Á., Oppenheimer B. D., Kraft R. P., Forman W. R., Jones C., 2022, ApJ, 936, L15
Choi E., Ostriker J. P., Naab T., Johansson P. H., 2012, ApJ, 754, 125
Comparat J. et al., 2022, A&A, 666, A156
Croston J. H. et al., 2019, A&A, 622, A10
Cui W. et al., 2018, MNRAS, 480, 2898
Cui W., Davé R., Peacock J. A., Anglés-Alcázar D., Yang X., 2021, Nat. Astron., 5, 1069
Cui W. et al., 2022, MNRAS, 514, 977
Davé R., Thompson R., Hopkins P. F., 2016, MNRAS, 462, 3265
Davé R., Anglés-Alcázar D., Narayanan D., Li Q., Rafieferantsoa M. H., Appleby S., 2019, MNRAS, 486, 2827
Davies J. J., Crain R. A., Oppenheimer B. D., Schaye J., 2020, MNRAS, 491, 4462
Fabian A. C., 2012, ARA&A, 50, 455
Ganeshaiah Veena P., Cautun M., van de Weygaert R., Tempel E., Jones B. J. T., Rieder S., Frenk C. S., 2018, MNRAS, 481, 414
Ganeshaiah Veena P., Cautun M., Tempel E., van de Weygaert R., Frenk C. S., 2019, MNRAS, 487, 1607
Giles P. A. et al., 2016, A&A, 592, A3
Guillard P., Boulanger F., Lehnert M. D., Pineau des Forêts G., Combes F., Falgarone E., Bernard-Salas J., 2015, A&A, 574, A32
Hafen Z. et al., 2022, MNRAS, 514, 5056
Harrison C. M., 2017, Nat. Astron., 1, 0165
Heckman T. M., Best P. N., 2014, ARA&A, 52, 589
Hlavacek-Larrondo J. et al., 2015, ApJ, 805, 35
Ho L. C., 2008, ARA&A, 46, 475
Hopkins P. F., 2015, MNRAS, 450, 53
Kacprzak G. G., Churchill C. W., Nielsen N. M., 2012, ApJ, 760, L7
Kakkad D. et al., 2020, A&A, 642, A147
Kakkad D. et al., 2023, MNRAS
Kauffmann G. et al., 2003, MNRAS, 346, 1055
Kennicutt R. C. J., 1998, ApJ, 498, 541
Kormendy J., Ho L. C., 2013, ARA&A, 51, 511
Kraft R. et al., 2022, preprint (arXiv:2211.09827)
Krumholz M. R., Gnedin N. Y., 2011, ApJ, 729, 36
Le Brun A. M. C., McCarthy I. G., Schaye J., Ponman T. J., 2014, MNRAS, 441, 1270
Liu W. et al., 2019, MNRAS, 484, 3376
Łokas E. L., Mamon G. A., 2001, MNRAS, 321, 155
Lokken M., Cui W., Bond J. R., Hložek R., Murray N., Davé R., van Engelen A., 2023, MNRAS, 523, 1346
Luo B. et al., 2017, ApJS, 228, 2
Maiolino R. et al., 2012, MNRAS, 425, L66
Martín-Navarro I., Pillepich A., Nelson D., Rodriguez-Gomez V., Donnari M., Hernquist L., Springel V., 2021, Nature, 594, 187
McCarthy I. G. et al., 2010, MNRAS, 406, 822
McCarthy I. G., Schaye J., Bird S., Le Brun A. M. C., 2017, MNRAS, 465, 2936
Meiksin A., Bolton J. S., Tittley E. R., 2014, MNRAS, 445, 2462
Meiksin A., Bolton J. S., Tittley E. R., 2015, MNRAS, 453, 899
Meiksin A., Bolton J. S., Puchwein E., 2017, MNRAS
Mitchell P. D., Schaye J., Bower R. G., Crain R. A., 2020, MNRAS, 494, 3971
Morganti R., 2017, Front. Astron. Space Sci., 4, 42
Muratov A. L., Kereš D., Faucher-Giguère C.-A., Hopkins P. F., Quataert E., Murray N., 2015, MNRAS, 454, 2691
Nandra K. et al., 2007, ApJ, 660, L11
Nelson D. et al., 2018, MNRAS, 477, 450
Nelson D. et al., 2019, MNRAS, 490, 3234
Nelson D., Byrohl C., Peroux C., Rubin K. H. R., Burchett J. N., 2021, MNRAS, 507, 4445

Nica A., Oppenheimer B. D., Crain R. A., Bogdán Á., Davies J. J., Forman W. R., Kraft R. P., ZuHone J. A., 2022, MNRAS, 517, 1958
Nielsen N. M., Churchill C. W., Kacprzak G. G., Murphy M. T., Evans J. L., 2015, ApJ, 812, 83
Oppenheimer B. D., Babul A., Bahé Y., Butsky I. S., McCarthy I. G., 2021, Universe, 7, 209
Orlowski-Scherer J. et al., 2022, A&A, 667, L6
Perna M., Lanzuisi G., Brusa M., Mignoli M., Cresci G., 2017a, A&A, 603, A99
Perna M., Lanzuisi G., Brusa M., Cresci G., Mignoli M., 2017b, A&A, 606, A96
Péroux C., Nelson D., van de Voort F., Pillepich A., Marinacci F., Vogelsberger M., Hernquist L., 2020, MNRAS, 499, 2462
Pillepich A. et al., 2018, MNRAS, 473, 4077
Pillepich A., Nelson D., Truong N., Weinberger R., Martin-Navarro I., Springel V., Faber S. M., Hernquist L., 2021, MNRAS, 508, 4667
Planck Collaboration XIII, 2016, A&A, 594, A13
Pović M. et al., 2012, A&A, 541, A118
Predehl P. et al., 2021, A&A, 647, A1
Putman M. E., Peek J. E. G., Joung M. R., 2012, ARA&A, 50, 491
Ramesh R., Nelson D., Pillepich A., 2023, MNRAS, 518, 5754
Rodríguez Montero F., Davé R., Wild V., Anglés-Alcázar D., Narayanan D., 2019, MNRAS, 490, 2139
Schawinski K., Thomas D., Sarzi M., Maraston C., Kaviraj S., Joo S.-J., Yi S. K., Silk J., 2007, MNRAS, 382, 1415
Schaye J. et al., 2015, MNRAS, 446, 521
Schellenberger G. et al., 2023, preprint (arXiv:2307.01259)
Sijacki D., Vogelsberger M., Genel S., Springel V., Torrey P., Snyder G. F., Nelson D., Hernquist L., 2015, MNRAS, 452, 575
Somerville R. S., Davé R., 2015, ARA&A, 53, 51
Sorini D., Oñorbe J., Hennawi J. F., Lukić Z., 2018, ApJ, 859, 125
Sorini D., Davé R., Anglés-Alcázar D., 2020, MNRAS, 499, 2760
Sorini D., Davé R., Cui W., Appleby S., 2022, MNRAS, 516, 883
Stern J., Fielding D., Hafen Z., Su K.-Y., Naor N., Faucher-Giguère C.-A., Quataert E., Bullock J., 2023, preprint (arXiv:2306.00092)
Terrazas B. A. et al., 2020, MNRAS, 493, 1888
Truong N. et al., 2020, MNRAS, 494, 549
Truong N., Pillepich A., Werner N., 2021a, MNRAS, 501, 2210
Truong N., Pillepich A., Nelson D., Werner N., Hernquist L., 2021b, MNRAS, 508, 1563
Truong N. et al., 2023, MNRAS
Tumlinson J., Peeples M. S., Werk J. K., 2017, ARA&A, 55, 389
Turner M. L., Schaye J., Steidel C. C., Rudie G. C., Strom A. L., 2014, MNRAS, 445, 794
Turner M. L., Schaye J., Crain R. A., Rudie G., Steidel C. C., Strom A., Theuns T., 2017, MNRAS, 471, 690
Weinberger R. et al., 2018, MNRAS, 479, 4056
Yang T., Cai Y.-C., Cui W., Davé R., Peacock J. A., Sorini D., 2022, MNRAS, 516, 4084
Zaritsky D., Smith R., Frenk C. S., White S. D. M., 1997, ApJ, 478, L53
Zinger E. et al., 2020, MNRAS, 499, 768

APPENDIX A: NUMERICAL CONVERGENCE

For the SIMBA -50-'allphys' model and the SIMBA -100 model, both runs implement the same feedback mechanisms and have identical numerical resolutions. Therefore, we want to see the sensitivity of the predicted CGM anisotropy to the finite simulation volume by testing whether the quadrupole curves measured from two 'allphys' models converge well.

Fig. A1 shows he resulting quadrupole curves around galaxies selected from the SIMBA -50-'allphys' model and the SIMBA -100 model, using all 'jet-active' galaxies with stellar masses between 1×10^{10} and 5×10^{10} $M_\odot$ at $z = 0.0$. Only results from the stacked edge-on $T_{\rm mw}$, $\Sigma_{\rm gas}$,and thermal SZ$-y$ maps are shown here for illustration. The shaded area shows the bootstrap errors around the average, where only error bars obtained from the the SIMBA -50-'allphys' are included. According to this plot, the general trends of CGM anisotropic features measured from two models are in good agreement with each other. Especially at $r \gtrsim 0.5 r_{200c}$ – the region where the cumulative effect of the jet is the most noticeable, the quadrupole values estimated from two models overlap reasonably well. Hence, we conclude that the resulting features of CGM anisotropy are not sensitive to the finite volume size.

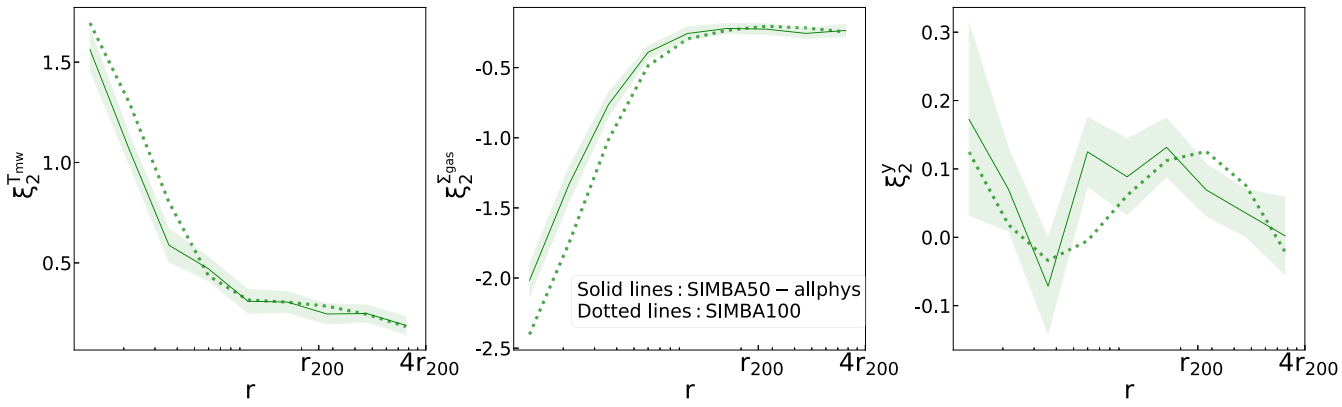

Figure A1. $T_{\rm mw}$, $\Sigma_{\rm gas}$, and thermal SZ$-y$ quadrupole curves measured around samples from the SIMBA -50-'allphys' (solid lines) and the SIMBA 100 model (dotted lines), using all 'jet-active' galaxies with stellar masses between 1×10^{10} and 5×10^{10} $M_\odot$ at $z = 0.0$. Only results from the edge-on projected maps are shown here. The shaded area shows the bootstrap errors around the average, where only error bars obtained from the SIMBA -50-'allphys' case are included.

APPENDIX B: EFFECT OF STACKING AXES

In this study, in order to exhibit the angular dependence of CGM properties, galaxies as well as their surrounding particle fields are stacked with respect to the minor axes of their inner gas discs, or 'jet-direction' around 'allphys' galaxies. However, this vector direction is hard to measure in real observations. An alternative is to choose the stellar angular momentum vector, which is computed using all stellar particles within the stellar half-mass radius around the galactic centre. In this section, we examine the sensitivity of the predicted CGM anisotropy to the reference axes that we stack against.

Fig. B1 shows the comparison of $T_{\rm mw}$ and $\Sigma_{\rm gas}$ quadrupole curves for galaxies from the SIMBA-100 model, measured on the edge-on projected maps stacked along the jet direction or along the stellar angular momentum vectors. Here, for illustration, we test the sensitivity of the resulting CGM anisotropy to the reference stacked axes around galaxies with different star formation status. The top row of Fig. B1, shows the results measured around 'jet-active' SIMBA-100 central galaxies at $z = 0.0$ within the stellar mass bin $M_* = (1\text{–}5) \times 10^{10}$ M$_\odot$. For comparison, the bottom row shows the results measured around all central galaxies with accretion rate > 0.0 within the identical stellar mass bin.

According to the figure, the general quadrupole trends and CGM features, especially at large distances, are in agreement with each other – regardless of stacking the galaxies along their jet or stellar angular momentum vectors. The two vectors for the star forming and the GV populations align reasonably well, with an average angle between them of $\sim 37^\circ$ for SF populations and $\sim 60^\circ$ for GV populations. For quenched populations, however, the average angle between the two vectors can reach $\sim 80^\circ$. Around quenched galaxies, it is highly possible that well-formed gaseous

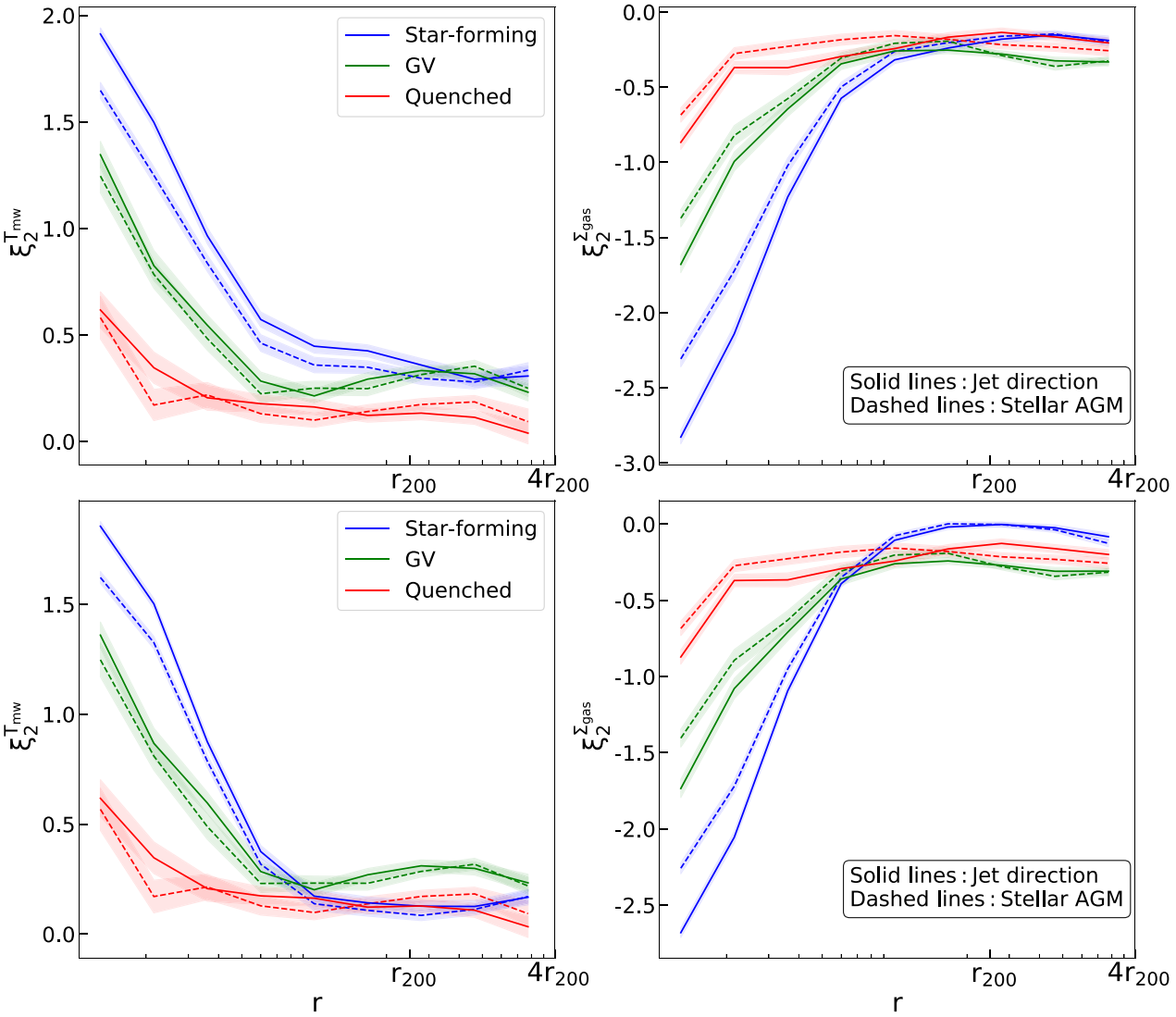

Figure B1. Comparison of $T_{\rm mw}$ and $\Sigma_{\rm gas}$ quadrupole curves for different galaxy types from the SIMBA-100 model (SF: blue, GV: green, Q: red) measured on the edge-on projected maps stacked along the jet direction (as shown in Fig. 3, solid lines) and along the stellar angular momentum vector, dashed line. Top row shows the results measured around all 'jet-active' central galaxies within stellar mass bin $M_* = (1 - 5) \times 10^{10}$ M$_\odot$, and the bottom row shows the results measured around all central galaxies with accretion rate > 0.0 within the same stellar mass bin. Shaded regions show the bootstrap errors.

and stellar discs are missing, so that their vector directions can have a more uniform distribution compared to their SF and GV counterparts. As shown in Section 3.1, the cumulative jet effect drives a more extended and isotropic hot gas distribution around the quenched galaxies, which makes them less sensitive to the choices of stacking axes in the inner region. Therefore, we conclude that the resulting CGM properties and their angular dependence in the stacked maps are insensitive to those two chosen axes. We leave a more thorough comparison with other choices of axes for future work.

This paper has been typeset from a TEX/LATEX file prepared by the author.